Research and Development of a Digital Hybrid Avalanche Photo-Detector

Wang, Jiayin

January 2012

Abstract

A new photosensor named the Hybrid Avalanche Photo-Detector (HAPD) and its dedicated readout system have been developed for next generation water Cherenkov detectors.

In this thesis, the performance of a newly developed "digital HAPD", a package of an HAPD, HV power supply and the readout system, is presented. A compact readout board and an HV supply, which can be installed on the back of HAPD, are developed. A digital HAPD requires only a low voltage power supply and a network cable. In addition, the new HAPD uses a glass structure instead of metal flanges to simplify its housing structure. The single photon detection capability is verified with an 8-inch digital HAPD.

A waveform sampler with Analog Memory Cell and Wilkinson ADCs implemented in a monolithic IC is developed to improve the performance of the digital HAPD. The functionality of the waveform sampler is verified, however, its resolution measured to be about 7 bit is worse than the design value of 10 bit and needs improvement and future study.

Contents

Chapter 1

Introduction

We report on the development of the digital Hybrid Avalanche Photo-Detector (HAPD) as a candidate for the photosensor to be used in next generation water Cherenkov detectors. After the discovery by Super-Kamiokande (Super-K) in 1998 [1],

neutrino oscillations have been regarded as phenomena which lead us to a theory beyond the Standard Model and studied with keen interest all over the world.

Neutrino oscillations were confirmed by the K2K experiment [2], the first long baseline neutrino oscillation experiment in the world making use of artificial neutrinos from an accelerator. Super-K [3, 4], SNO [5], and KamLAND [6, 7] revealed that neutrino oscillations are also responsible for the deficit in solar neutrino observations. Recently, the T2K experiment has reported indications of the third and last type of neutrino oscillation using an accelerator neutrino beam and the Super-K detector.

The next target of experimental neutrino physics is to discover the CP asymmetry, i.e. the difference between particles and anti-particles, in the neutrino sector.

In order to observe CP violation in the neutrino sector, we need to measure the difference in oscillation probabilities between neutrino and anti-neutrino. This requires a larger number of neutrino events than those possible with existing detectors. Therefore, a larger detector will be necessary for observation of leptonic CP violation. Moreover, much larger detectors are essential for the search of nucleon decay, another major goal of experimental particle physics.

In order to achieve these goals, there are several projects proposed to construct Mega-ton class neutrino detectors around the world. In Japan, Hyper-Kamiokande (Hyper-K) [8], which is a water Cherenkov detector with approximately 20 times larger volume than Super-K, has been studied. Assuming a photocathode coverage of 20%, approximately 100,000 photosensors are needed. This calls for development of a new type of photosensor which is easier to produce and maintain.

The photosensors must be able to detect Cherenkov radiation emitted by

charged particles with accuracy to reconstruct the neutrino events precisely. The requirements to the photosensors are that

- they can detect single-photon signals,
- their time resolution is better than 1 ns,
- they have a large photocathode with high quantum efficiency, and
- they have a wide input dynamic range up to ∼300 photoelectrons.

We have been developing Hybrid Avalanche Photo-Detectors (HAPDs) together with dedicated readout systems as a candidate for the photosensor to be employed in next generation water Cherenkov detectors. HAPDs can detect single-photon signals and their time resolution is better than that of Photo-Multiplier Tubes (PMT) being used for neutrino experiments so far.

In this thesis, development of a digital HAPD, which is a package including an HAPD, a readout system and a high voltage supply, is described. The digital HAPD has been developed to reduce the cost in mass production and to make the device more user friendly.

The motivation for our R&D and the principles of HAPDs are discussed in Chapter 2. The performances of HAPDs which have been evaluated before this thesis work are summarized in Chapter 3 to show how HAPDs satisfy basic requirements. In Chapter 4, we describe the performance of a digital HAPD. In Chapter 5, we report on the current status of R&D of a new readout system for digital HAPDs. We summarize the study in Chapter 6.

Chapter 2

The background and motivation for our R&D

In this chapter, we describe the physics motivation for our study, requirements for the photosensors in next generation water Cherenkov detectors and why we choose HAPD as a candidate to meet the requirements.

2.1 Physics motivations

In this section, we explain the physics motivations for our study. First, we explain what are neutrino oscillations and why they have attracted so much interest. Then, we discuss how we use water Cherenkov detectors to study the property of neutrinos and the requirements for photosensors in next generation water Cherenkov detectors.

2.1.1 Neutrino oscillations and their mass

Neutrinos are elementary particles which make up matter in our universe. They are categorized as leptons since they do not have color charge to interact with other particles strongly. They are distinguished from charged leptons, i.e. electrons, muons, and taus, because they do not have electric charge. In effect, the only way to directly detect them is to make them interact with matter weakly, which means we can only grasp a scent of them even though they are one of the most abundant particles in our universe.

All the particles categorized as leptons are shown in Table 2.1.

The generations of leptons are observables and called "flavors," which represent the eigenstates of weak interactions.

Neutrinos are created and detected as eigenstates of the Hamiltonian of weak interactions. However, the time evolution during their propagation in space obeys their free Hamiltonians. Because the free Hamiltonians and the Hamiltonian of weak interactions are not compatible, the detected flavor of

Table 2.1: Table of leptons. Neutrinos are different with charged leptons in electric charges they possess. There are three generations in both charged leptons and neutrinos. We call the generations "flavors."

generation	1	2	3	electric charge $[e]$
charged leptons	e	μ	τ	-1
neutrinos	ν_e	ν_μ	ν_τ	0

neutrinos can be different, in a certain probability, from that at the time when they were generated. We call this phenomenon "neutrino oscillation."

If we write the three eigenstates of the free Hamiltonian $\hat{H}_{\text{free}}$ (Hamiltonian of the weak interaction $\hat{H}_{\text{int}}$) as $\nu_i\,(i=1,2,3)$ ($\nu_\alpha\,(\alpha=e,\mu,\tau)$), and the eigenvalues of the three eigenstates of $\hat{H}_{\text{free}}$ as $E_i\,(i=1,2,3)$, respectively, then ν_α can be written as

$$\begin{pmatrix}\nu_e\\ \nu_\mu\\ \nu_\tau\end{pmatrix} = \begin{pmatrix}U_{e1} & U_{e2} & U_{e3}\\ U_{\mu1} & U_{\mu2} & U_{\mu3}\\ U_{\tau1} & U_{\tau2} & U_{\tau3}\end{pmatrix}\begin{pmatrix}\nu_1\\ \nu_2\\ \nu_3\end{pmatrix}, \tag{2.1.1}$$

where $\hat{U} = (U_{\alpha i})$ is Pontecorvo-Maki-Nakagawa-Sakata (PMNS) mixing matrix [9, 10]. We apply Schrödinger equation to

$$\nu_\alpha\,(t=t_0) = \sum_i U_{\alpha i}\nu_i \tag{2.1.2}$$

and get

$$\nu_\alpha\,(t=t_0+\Delta t) = \sum_i U_{\alpha i}e^{-iE_i\Delta t}\nu_i. \tag{2.1.3}$$

Thus, we can calculate the probability, $\text{Prob}\,(\nu_\alpha\to\nu_\beta)$, that a neutrino generated in a initial state of ν_α is observed in a final state of ν_β as follows.

$$\begin{aligned}
&\text{Prob}\,(\nu_\alpha\to\nu_\beta) && (2.1.4)\\
&= \left|\langle\nu_\beta\,(t_0+\Delta t)\,,\nu_\alpha\,(t_0)\rangle\right|^2 && (2.1.5)\\
&= \left|\left\langle\sum_i U_{\beta i}e^{-iE_i\Delta t}\nu_i, \sum_i U_{\alpha i}\nu_i\right\rangle\right|^2 && (2.1.6)\\
&= \sum_i |U_{\alpha i}U_{\beta i}|^2 + \sum_{i\neq j} U_{\alpha i}U^*_{\beta i}U^*_{\alpha j}U_{\beta j}e^{-i(E_i-E_j)\Delta t}. && (2.1.7)
\end{aligned}$$

This phenomenon is named neutrino "oscillation" because the transition probability $\text{Prob}\,(\nu_\alpha\to\nu_\beta)$ oscillates as time passes by.

Close examination of the oscillation probabilities tells us a lot about the properties of the neutrino sector because there appear seven valuable quantities to be determined in the transition probabilities.

The eigenvalues E_i can be expressed as

$$E_i = \sqrt{p_i^2 + m_i^2} \tag{2.1.8}$$

$$\simeq p_i \left(1 + \frac{1}{2}\frac{m_i^2}{p_i^2}\right), \tag{2.1.9}$$

given $|m_i/p_i| \ll 1$.

$$E_i - E_j \propto \frac{m_i^2 - m_j^2}{p} \tag{2.1.10}$$

where $p_i = p$ is the momentum and m_i is the mass eigenvalues of a neutrino. In order for neutrino oscillation to happen, at least one of the neutrino mass eigenvalues must be nonzero. Therefore, the discovery of neutrino oscillation by Super-K in 1998 was the first evidence of non-zero neutrino mass.

2.1.2 Leptonic CP violation

Discovery of CP asymmetry, i.e. the difference between particles and anti-particles, in the lepton sector is a big goal in neutrino physics.

If a neutrino ν_α and an anti-neutrino $\bar{\nu}_\alpha$ is not perfectly CP-symmetrical, there should be differences in transition probabilities $\mathrm{Prob}\,(\nu_\alpha \to \nu_\beta)$ and $\mathrm{Prob}\,(\bar{\nu}_\alpha \to \bar{\nu}_\beta)$ $(\alpha \neq \beta)$.

We can measure the transition probabilities by producing neutrino and anti-neutrino beams of a specific flavor, shooting them into a distant detector, letting neutrinos in the beam oscillate and distinguishing the flavor of the observed neutrinos.

With current experimental techniques, $\nu_\mu\,(\bar{\nu}_\mu) \to \nu_\mathrm{e}\,(\bar{\nu}_\mathrm{e})$ is the most promising channel to detect the difference in transition probabilities. In order to find the difference in transition probabilities, a large statistics of neutrino events is needed. We regard a water Cherenkov detector as one of the best candidates for the distant detector from the viewpoint of the feasibility to prepare a large target and the ability to distinguish electron neutrinos from muon neutrinos.

2.2 Water Cherenkov detectors

We explain the principle of water Cherenkov detectors, the future plan of next generation water Cherenkov detectors, and the requirements for photosensors to be used in them.

2.2.1 The principle of water Cherenkov detectors

In recent decades, large water Cherenkov detectors represented by Super-K have acquired a great number of monumental accomplishment, such as the discovery of neutrino oscillation in the atmospheric neutrino, the solution to the solar neutrino deficit, the observation of appearance and disappearance of accelerator neutrinos, and the setting of the best limits to the lifetime of protons.

Water Cherenkov detectors mainly consist of a large tank to store ultra-pure water and a large number of photosensors on the wall of the tank. When an incident particle with electric charge enters the ultra-pure water and travels faster than the speed of light in the water, it emits Cherenkov light which propagates at a constant angle θ specific to the velocity of the incident particle, which can be written as

$$\cos\theta = \frac{1}{\beta n}, \tag{2.2.1}$$

where β is the speed of the incident particle with unit of c and $n = 1.33$ is the refractive index of water. The photosensors detect the Cherenkov light in a ring pattern, and one can identify the type of the incident particle and reconstruct the energy-momentum vector of it using the shape of the ring and the total amount of light.

Water Cherenkov detectors have an advantage in that it is easier to prepare a target with large effective volume than other detectors such as liquid scintillators or liquid argon time projection chambers, and that they have 4π solid angle coverage. These two properties are essential to detect the rare neutrino interactions with high statistics and high efficiency.

2.2.2 Next generation water Cherenkov detectors

As the next generation experiments, several projects to construct water Cherenkov detectors with a total volume of the order of Mega-ton are underway around the world. In Japan, Hyper-Kamiokande detector (Hyper-K) with 20 (25) times larger total (fiducial) volume than Super-K is proposed. With the current design, approximately 100,000 photosensors are needed (Fig. 2.1). Development of a new photo-sensor is one of key R&D items to realize such a detector.

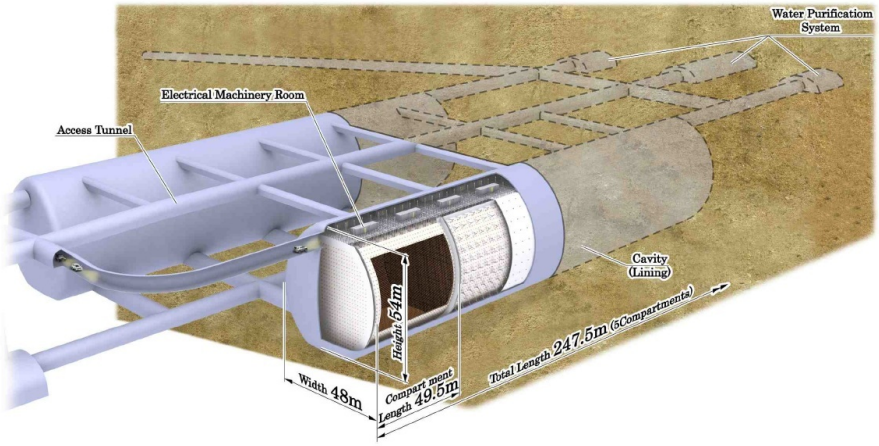

Figure 2.1: Schematic diagram of the Hyper-Kamiokande detector [8].

2.2.3 Requirements for photosensors

Major requirements for the performances of photosensors to be used in next generation water Cherenkov detectors are that they have

1. a simple structure,
2. a time resolution better than 1 ns,
3. a pulse-height resolution good enough to distinguish single-photon signals,
4. a large photocathode, and
5. a wide dynamic range up to $\sim$ 300 photoelectrons.

The first one is important for cost reduction in mass production. The second one is essential to reconstruct the position where neutrino interaction occurs (the vertex of neutrino interaction). The better the time resolution is, the better the vertex reconstruction becomes. Considering the time resolution of PMTs used in Super-K is 1.4 ns, our requirement of the time resolution being better than 1 ns is reasonable as the first step of aimed improvement. The third and fourth are required to achieve good energy reconstructions and ring pattern recognitions, and the last one enables the apparatus to detect neutrinos with high energy.

We adopt large aperture Hybrid Avalanche Photo-Detectors (HAPD) as a candidate for photosensors in next generation water Cherenkov detectors. HAPDs are created by combining the technology of semiconductors and photo-multiplier tubes (PMTs). The major difference between HAPDs and PMTs is that HAPDs substitute avalanche diode for dynodes in PMTs to multiply the photo-electrons. HAPDs are much simpler in structure because they do not have dynodes, have a better time resolution, are sensitive to single-photon signals,

can be equipped with a large photocathode, and have a wide dynamic range. We have developed HAPDs because they are promising to meet the major requirements as a photosensor to be used in next generation water Cherenkov detectors.

2.3 Overview of HAPDs

In this section, we make a short introduction to the history of Hybrid Photo-Detectors (HPDs) and describe the principle and properties from the viewpoint of HAPDs' structure.

2.3.1 The history of HPD

It was in early 1960's that semiconductor devices were found to have sensitivity to ionizing particles. When a charged particle hits the semiconductor and enters the depletion region of P-N junction with inverted bias, it creates pairs of electron and holes, and the information about the incident particle can be obtained by reading them out electrically.

If the incident particle is an electron whose energy is low enough that the electron loses all the energy and stops in the semiconductor, the number of electron-hole pairs is proportional to the energy it possesses. This process can be regarded as multiplication of electrons and the gain of it is named "bombardment gain."

Knowing this multiplication effect, F. A. White and J. C. Shefield suggested that a new type of photosensor can be created by combining a photocathode and the semiconductor devices, which is called "Hybrid Photo-Detector [11]."

However, it was not until 1987 that R. DeSalvo cast light on HPDs and used them as photosensors in a particle physics experiment [12]. After step-by-step researches and developments, HPDs come to be candidates for photosensors to be used in some experiments being underway.

2.3.2 HPD with an avalanche diode

Avalanche diode is named after its intrinsic multiplication function. By using an avalanche diode in an HPD, the detector can have higher gain than ordinary HPDs by approximately two orders. This type of HPD is called an "HAPD" and is useful because it can detect single-photon signals, which means it has possibility to replace PMTs in the future.

2.3.3 The structure of HAPD and its principle

Both HAPDs and PMTs utilize a set of photocathode and vacuum tube, but HAPDs are quite different from PMTs in the way they amplify signals.

A PMT amplifies the primary photoelectrons emitted from the photocathode by hammering them into a series of dynodes one after the other. Although a

single stage of dynode can only amplify the signal about five times, by allocating a cascade of dynodes to the appropriate position and letting multiplication occur repeatedly the total gain of secondary emitted electrons reaches 10^7.

On the other hand, an HAPD, which is not equipped with dynodes, accelerates electrons emitted from its photocathode in a strong electrostatic field between the photocathode and the semiconductor device, typically whose potential difference is 10-20 kV, and drive them into the avalanche diode. Those electrons lose their kinetic energy as they enter the depletion region of the avalanche diode and generate electron-hole pairs, the number of which is proportional to energy deposit. In the case of accelerating the primary electrons with an electrostatic field of 20 kV, approximately 4,500 electron-hole pairs are produced per every single incident electron (this process is called "bombardment multiplication"). Moreover, an avalanche diode in itself has an intrinsic ability to multiply electrons about 30 times (this process is called "avalanche multiplication"). In total, an HAPD has a gain of $\sim 10^5$, which makes the detection of single-photon event possible. A schematic drawing of an HAPD is in Fig. 2.2, in which the conceptual view of bombardment and avalanche multiplication is shown.

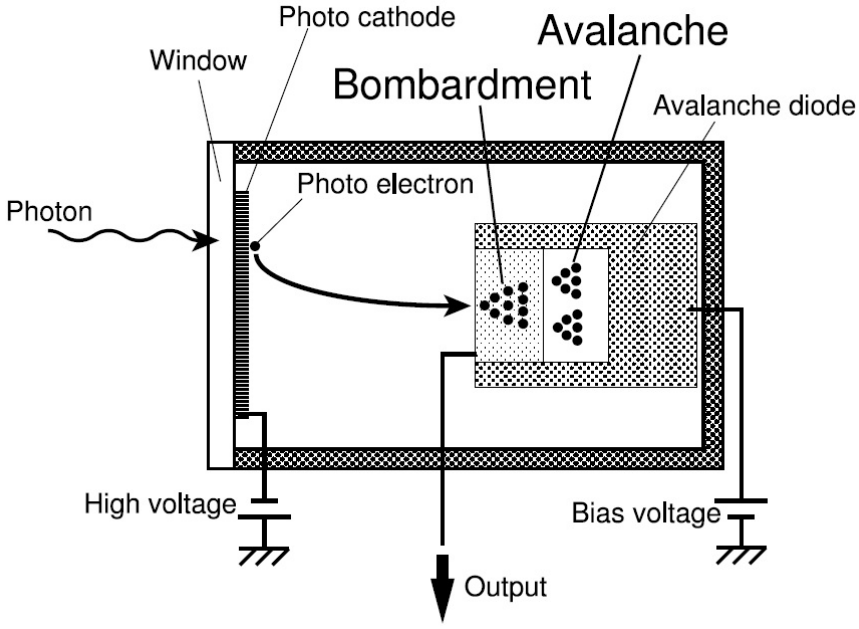

Figure 2.2: A schematic diagram of HAPD [13].

2.3.4 Expected Characteristics of HAPDs

We list up characteristics of HAPDs expected from its principle and structure.

Pros

Quality control and cost reduction It should be easier than PMTs to control the quality of HAPDs and reduce the cost through mass production because their structure is much simpler than that of PMTs.

Time resolution HAPDs have better time resolution compared to PMTs due to the uniformity of the path lengths of photoelectrons traveling from photocathode to avalanche diode.

Clean photon counting Since the first stage of multiplication has an essential effect on the ability to count photons, HAPDs' very small gain fluctuation in the stage of bombardment multiplication enables us to count photons very clearly, while PMTs' gain fluctuation is quite large.

Cons

Smaller gain compared to PMTs Because total gain of an HAPD is smaller than that of a PMT by two orders, HAPDs require a low noise readout system.

Higher operation voltage To operate HAPDs, we have to supply the apparatus with much higher voltage than PMTs, hence we should treat insulation very carefully.

Chapter 3

Large aperture HAPD

In recent years, HAPDs with photocathodes up to 13 inches in diameter have been developed.

We summarize the performance of large aperture HAPDs developed so far in this chapter. A photograph and a schematic diagram of the 13-inch HAPD are shown in Fig. 3.1. The performance described in this chapter is for the 13-inch HAPD [13, 14, 15].

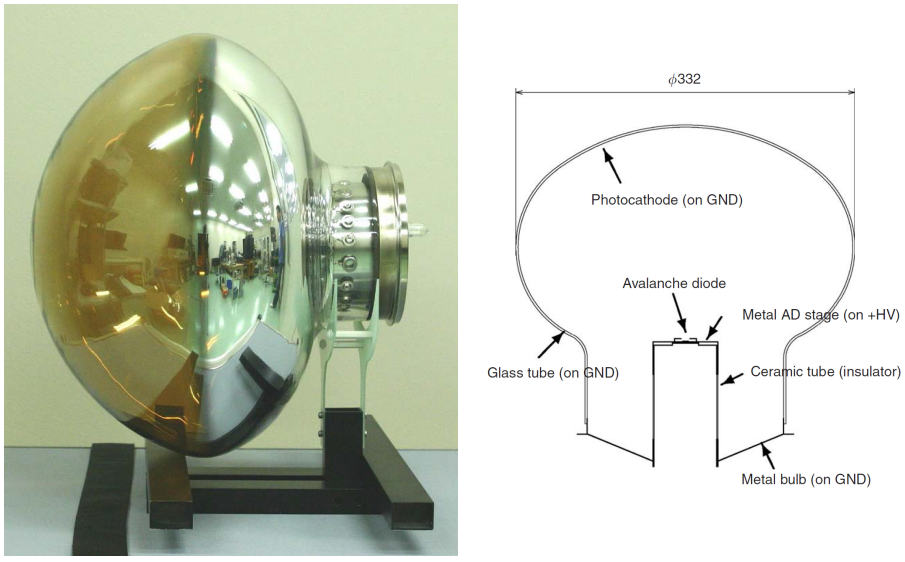

Figure 3.1: Left: A photograph of a 13-inch HAPD. Right: A schematic diagram of a 13-inch HAPD [16].

3.1 Multiplication gain of HAPD

The effective detection of single photon calls for 10^5 total gain of amplified signal. We measured bombardment gain and avalanche gain respectively to confirm that the total gain of our HAPDs reaches 2×10^5, given an electrostatic field of 20 kV between photocathode and avalanche diode and 390 V of bias voltage for avalanche diode.

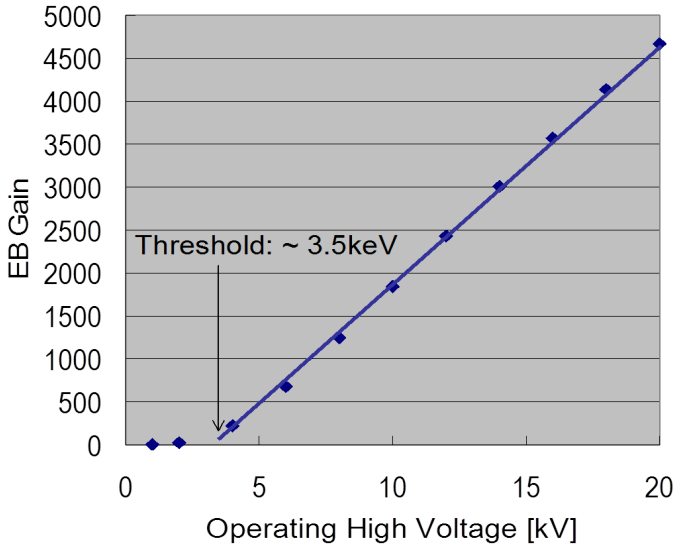

Figure 3.2: Bombardment gain vs. high voltage applied between the photocathode and the avalanche diode (bias voltage on avalanche diode was kept to be 30 V).

3.1.1 Bombardment gain

Figure 3.2 shows the measured bombardment gain as a function of the electrical potential difference between photocathode and avalanche diode. The bombardment gain is unity with the applied voltage below 3.5 kV because photoelectrons do not have enough kinetic energy to reach the depletion region of the avalanche diode. The bombardment gain increases proportionally to the high voltage once the photoelectrons reach the sensitive region. The bombardment gain reaches around 4,500 when the high voltage is set to be 20 kV.

3.1.2 Avalanche gain

The larger the area of avalanche diode is, the better the collection efficiency becomes. However, the increase in area leads to larger detector capacitance,

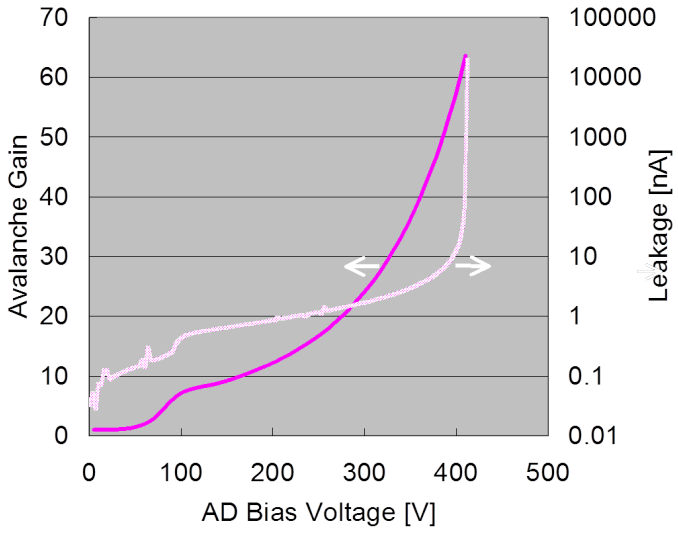

Figure 3.3: Avalanche gain vs. bias voltage (high voltage between photocathode and avalanche diode was kept to be 10 kV).

which may result in generating more noise. We optimized design parameters of avalanche diodes to achieve the aimed performance.

Figure 3.3 illustrates measured avalanche gain as a function of bias voltage put on the avalanche diode itself. The avalanche gain is approximately 50 with bias voltage of 390 V.

3.1.3 Total gain

The total gain ($\sim 2 \times 10^5$) fulfills the requirement of total gain over 10^5. The single photon signal can be distinguished as shown in Fig. 3.4.

3.2 Single photon detection performance

We have evaluated the signal height resolution for single photons. The pulse height resolution is 11 %. Figure 3.5 shows that the signal is clearly separated from noise.

Figure 3.6 shows the timing resolution of a single photon event captured by the HAPD, which is 190 ps.

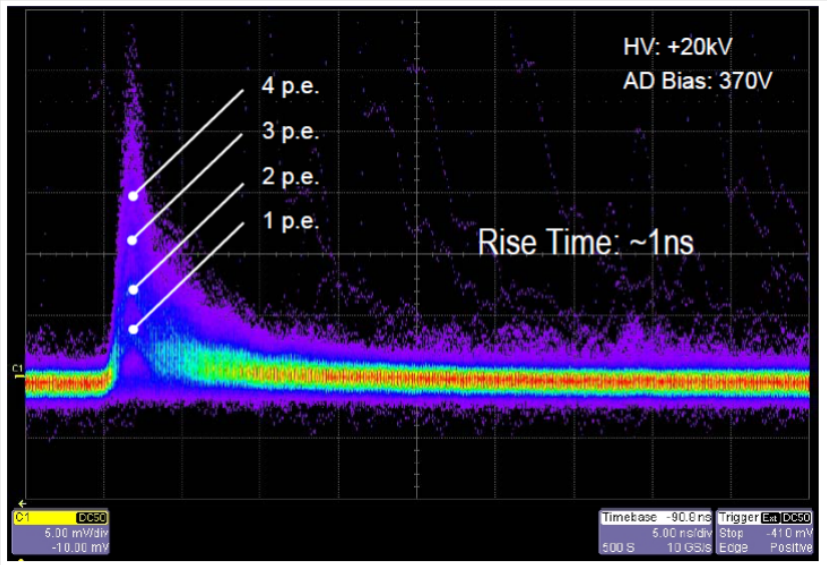

Figure 3.4: Signal shape from HAPD read on an oscilloscope (x-axis: 5 ns/div, y-axis: 6 mV/div).

3.3 Design of an electrostatic field structure

The uniformity of the length of photoelectrons' trajectories through which they are addressed to the avalanche diode plays a crucial role in realizing a good timing resolution. Moreover, stabilization of collecting efficiency of photoelectrons and the total gain are essential to the pulse height resolution.

We carefully designed the shape of the effective photocathode and the electrostatic field structure for acceleration and collection in order to minimize the fluctuation of photoelectrons' transit time (Cathode Transit Time Difference: CTTD) in which they travel from photocathode to avalanche diode and to maximize the collecting efficiency.

The fluctuation of total gain due to the difference in positions where the incident electrons enter the photocathode surface is measured to be less than 2% , which is sufficiently smaller than the pulse height resolution (11 %).

The largest CTTD value is approximately 500 ps and meets our requirement of <1 ns (Fig. 3.7).

Furthermore, we have carried out a computer simulation to get the collection efficiency of photoelectrons. According to the simulation, the collection efficiency is more than 95 % if the high voltage applied between photocathode and avalanche diode is above 15 kV (Fig. 3.8). The reason the collection efficiency of HAPDs is better than that of PMTs (∼70%) is that HAPDs have much simpler structure.

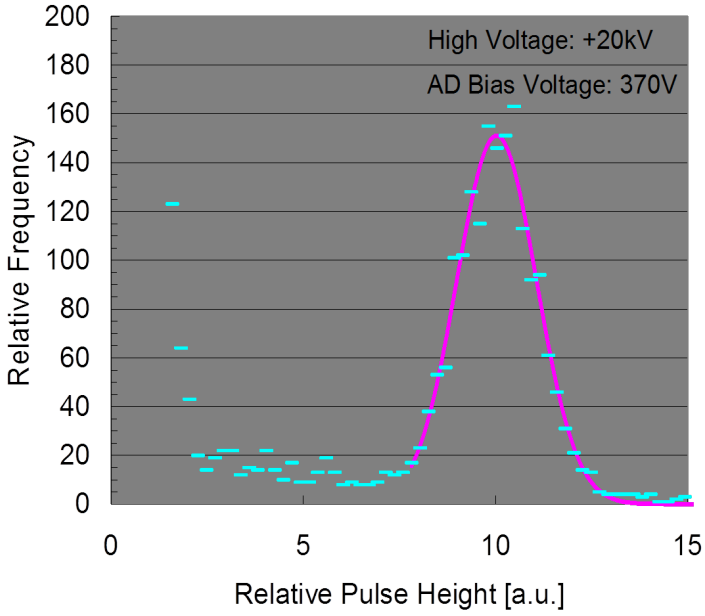

Figure 3.5: Signal height distribution of a single-photon event captured by HAPD.

3.4 Performance comparison between HAPDs and PMTs

We summarize the performance of large aperture HAPDs and PMTs in Table 3.1.

HAPDs has 7-time and 3-time better resolution of timing and pulse height, respectively, than PMTs. However, their total gain is two orders lower than that of PMTs. To compensate it, a dedicated readout system with low noise is indispensable. We discuss this topic in the next section.

3.5 HAPD readout system

We have adopted high-speed waveform sampling and digital signal processing to suppress noise. The schematic diagram of the readout system is shown in Fig. 3.9.

3.5.1 Pre-amplifier

A pre-amplifier is responsible for amplifying the charge signal from HAPDs and converting it into voltage information. Because of its relatively low gain of $\sim 10^5$

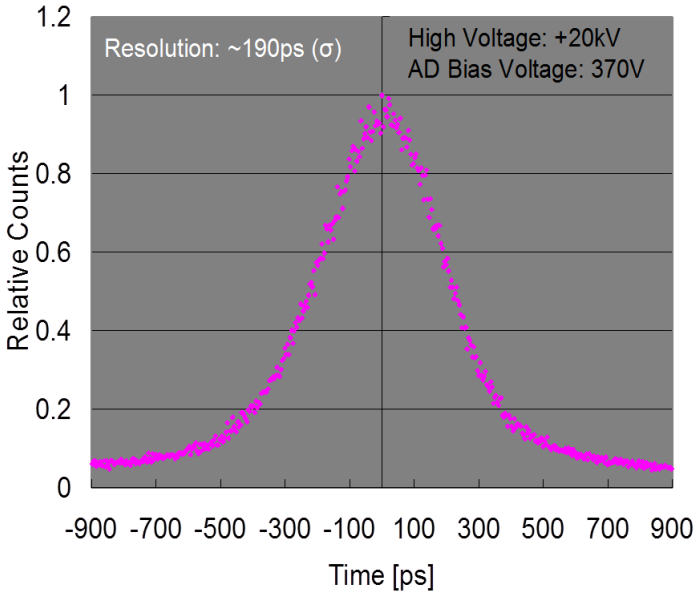

Figure 3.6: Timing resolution of a single-photon event captured by HAPD.

Table 3.1: Summary of performances of large aperture HAPDs and PMTs.

Parameters	13-inch HAPD	13-inch PMT	20-inch PMT
Number of structure units	∼300	∼3,000	∼3,000
Timing resolution (1 P.E.) [ps]	190	1,400	2,300
Pulse height resolution (1 P.E.) [%]	24	70	150
Dynamic range [P.E.]	3,000	1,000	1,000
Quantum efficiency [%]	20	20	20
Collection efficiency [%]	97	70	70
Power consumption [mW]	$\ll 700$	700	700
Total gain	10^5	10^7	10^7

and quick rise time of the signal pulse of several nano seconds, we must keep the noise coming from our pre-amplifier less than several thousand electrons in Equivalent Noise Charge (ENC).

The intrinsic noise of our pre-amplifier implemented with Application Specific Integrated Circuit (ASIC) is 3,400 electrons in ENC, given the detector capacitance is 40 pF. Thus, the Signal to Noise Ratio (S/N) of the signal coming from HAPD is $= 10^5/3400 \simeq 30$, which is good enough to detect single-photon signals.

3.5.2 Analog Memory Cell (AMC)

We use an Analog Memory Cell (AMC) to realize the high-speed waveform sampler. The large amount of power consumption of flash ADCs prevent us

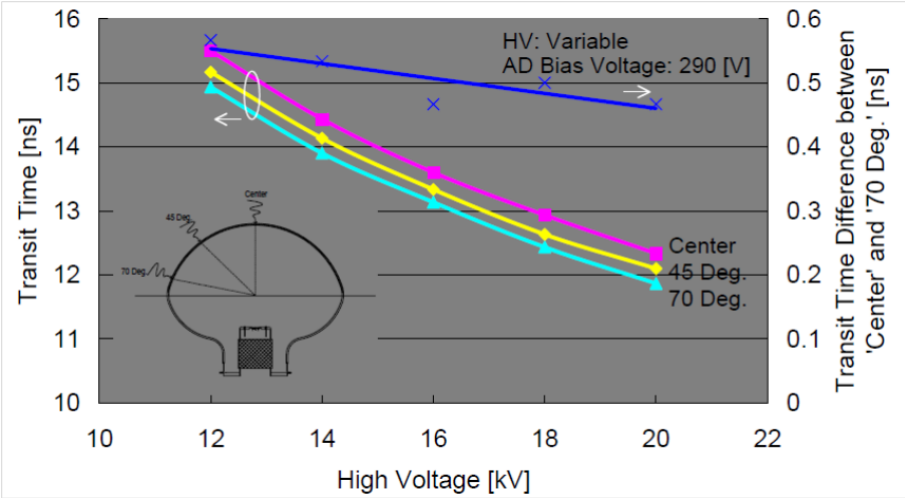

Figure 3.7: Cathode Transit Time Difference (CTTD).

from adopting them as waveform sampler because we need to place hundreds of thousands of HAPDs in Mega-ton class water Cherenkov detectors and the power consumption must be kept low.

The schematic diagram of an AMC is shown in Fig. 3.10. AMC consists of a pipeline of cell capacitors, delayed buffer for switches, analog multiplexer etc. By switching the capacitors on and off one after the other with triggers generated in delayed buffer, we can store the voltage information from pre-amplifier as electric charges in each capacitor in a very short constant interval of time without any high frequency clock signal.

Table 3.2: Performance comparison between AMC and existing flash ADC.

Parameters	AMC (w/ slow ADC)	Flash ADC (ADC081000)
Sampling frequency [GHz]	∼1	∼1
Voltage of power supply [V]	+5	+1.9
Power consumption [mW]	72 (+160 for ADC)	1450
Resolution [bit]	>10	8

We developed our AMC with 0.5 μm process provided by Taiwan Semiconductor Manufacturing Company. The evaluation of fundamental performances was carried out and summarized in Table 3.2. The dynamic range of AMC's output voltage is measured to be $\sim$ 2 V. The AMC has 11-bit resolution. The sampling interval is $\sim$ 800 ps (=1.25 GHz). Its power consumption of $<$ 250 mW (including slow ADC for digitization of output from cell capacitors) is much lower than that of flash ADCs operating at the similar sampling rate.

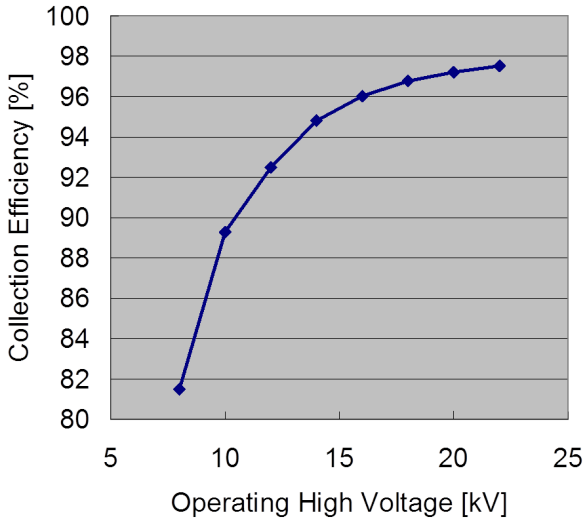

Figure 3.8: Simulation for collection efficiency of photoelectrons.

3.5.3 Digital circuit

The digital part of the readout system is responsible for

1. applying digital signal processing to digitized data from the waveform sampler to extract clean information, and

2. transmitting the extracted information of charge and time distributions.

A digital circuit named "FINENET" was developed to fit these demands. It has two FPGAs one of which is dedicated to digital signal processing and the other to controlling the Ethernet. Output of extracted information through Ethernet is incarnated with SiTCP technologies. We implemented the quick waveform sampler realized with AMC on FINENET to compose the whole readout system (see Fig. 3.11).

3.5.4 Performance

We evaluated performances of the entire system of the developed HAPD with low-noise readout circuit. The setup and result of the integration test is shown in Fig. 3.12 and 3.13, respectively. The charge distribution in Fig. 3.13 shows that our HAPD system can successfully distinguish the number of incident photons up to six-photoelectron signals. Moreover, the time resolution is approximately 200 ps for single photon signals. We have successfully developed the HAPD with readout system.

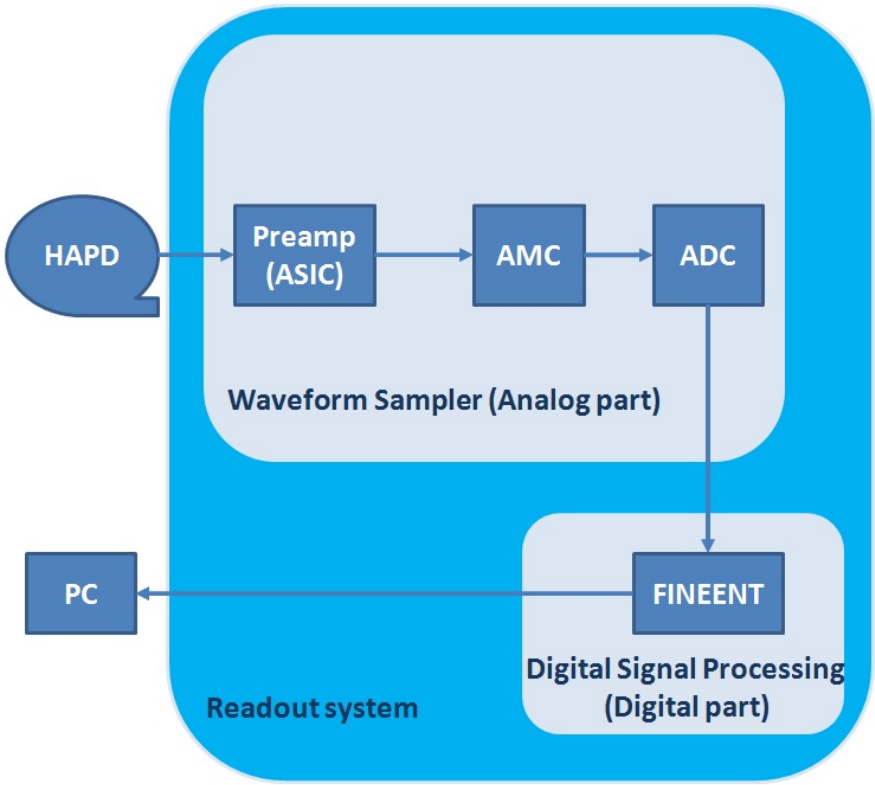

Figure 3.9: Schematic diagram of the readout system.

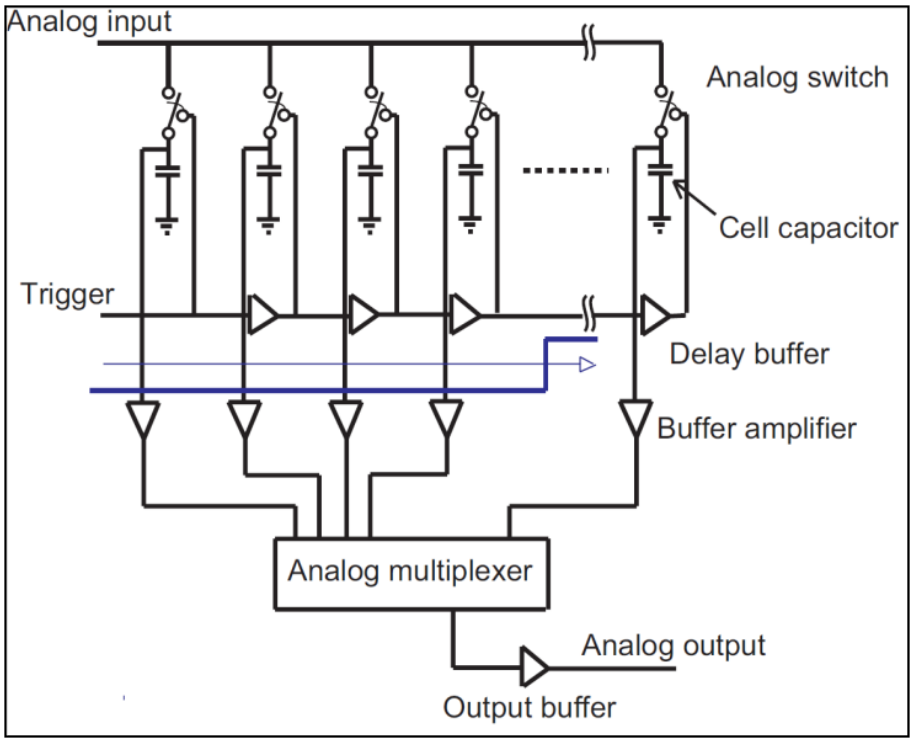

Figure 3.10: The equivalent circuit of AMC.

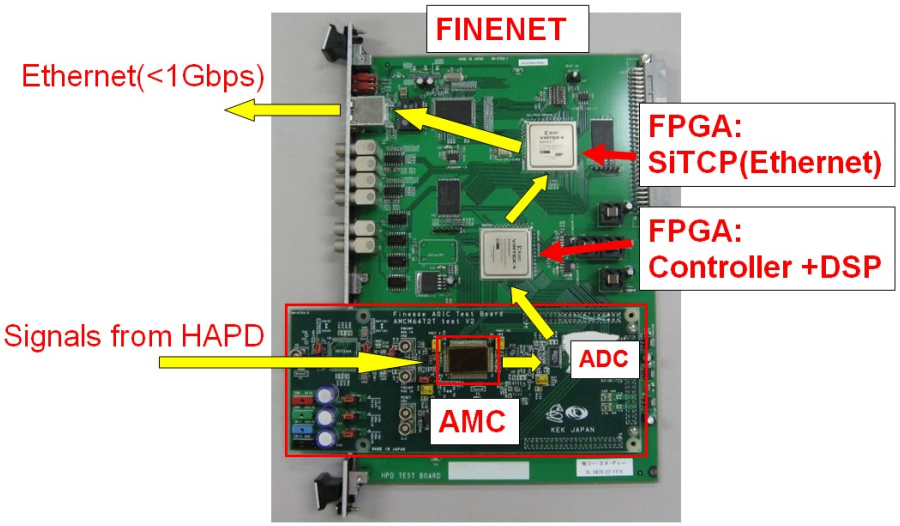

Figure 3.11: Overview of the readout system.

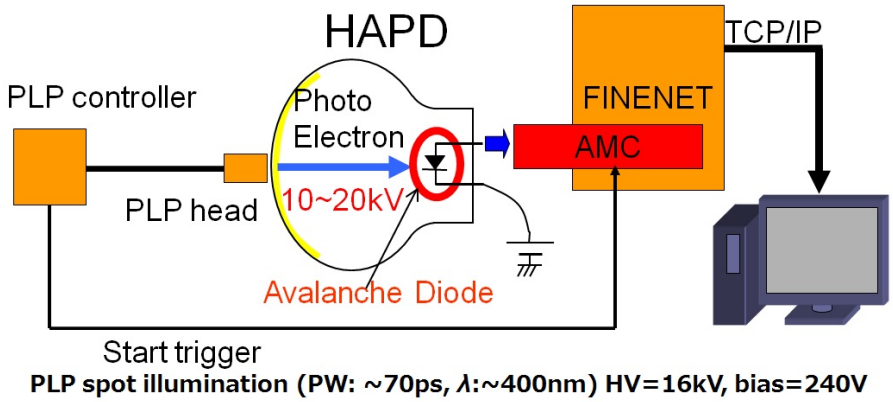

Figure 3.12: The setup of the integration test.

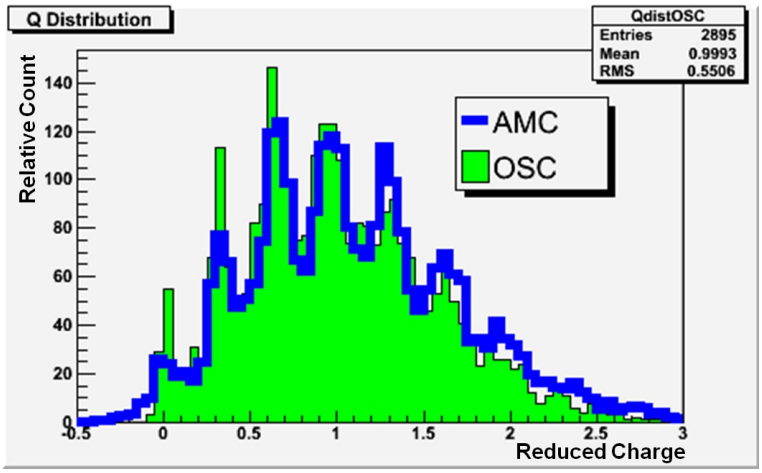

Figure 3.13: Charge distribution derived from the test of an HAPD and our readout system. The histogram and the solid line represent data read with an oscilloscope and our waveform sampler, respectively.

Chapter 4

Development of digital HAPD

We report on the R&D of "digital HAPD," which is a package consisting of an HAPD, a readout system and a HV power supply. We explain the motivation to develop the digital HAPD, its design and basic performance.

4.1 Digital HAPD

The motivations of the R&D and the main differences between a digital HAPD and an ordinary one are described in this section.

4.1.1 Motivation of development

As is described in the previous chapter, the large aperture HAPD is proven to meet the basic requirements for a photosensor to be used in next generation water Cherenkov detectors.

In order to be used in a real experiment, HAPDs must be easy to use and available at a reasonable price. We have been developing an 8-inch digital HAPD to meet these requirements. The size of 8 inch is chosen to be useful for other applications other than huge water Cherenkov experiments.

4.1.2 What is a digital HAPD

A digital HAPD is a package which includes an HAPD, a readout system and a HV power supply. By only connecting a power supply cable and a network cable to a digital HAPD, one can get digitized output from it.

Design of a digital HAPD

A photograph of the 8-inch digital HAPD is shown in Fig. 4.1. The readout system and the HV power supply are all installed on the back of the 8-inch

HAPD. One can use this to detect photons at ease just by connecting the sockets of the network and power cables.

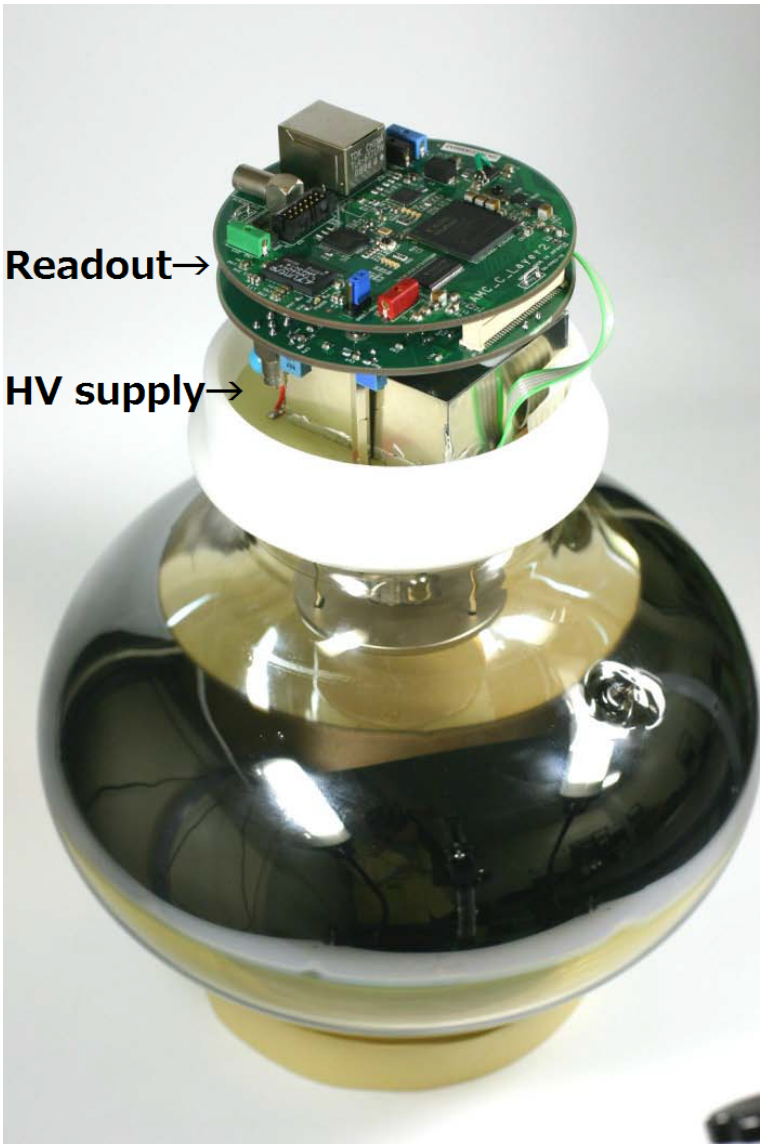

Figure 4.1: A photograph of an 8-inch digital HAPD.

The readout system includes a pre-amplifier, a waveform sampler composed of an AMC and ADCs, and a digital output controller implemented with FPGA. The outer dimensions of the previous readout board was $\sim 150 \times 250 \times 10\,\mathrm{mm}^3$, while the new board is ~ 8 cm in diameter (see Fig. 4.2). The outer dimensions

of the HV power supply used for the previous HAPDs were $\sim 150 \times 100 \times 30\,\mathrm{mm}^3$. The new HV supply for the digital HAPD has dimensions of $\sim 50 \times 50 \times 25\,\mathrm{mm}^3$ (see Fig. 4.3).

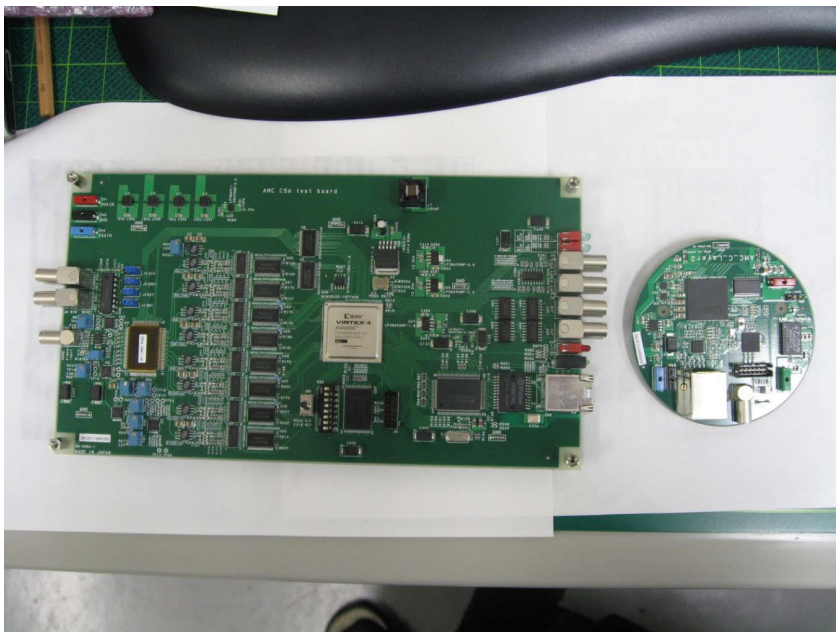

Figure 4.2: Comparison between the readout system of the digital HAPD and an ordinary one. The right is the readout system for the digital HAPD.

All-glass HAPD

In addition to the all-in-one package design, the new 8-inch HAPD has an improved structure. In order to simplify the structure and reduce the cost, we substituted a glass structure for the metal flanges used in previous versions of HAPDs. The number of components is reduced to be 6 from 10 of the one with metal flanges. The difference in appearance is shown in Fig. 4.4.

4.2 Performance of digital HAPD

The performance of the digital HAPD is reported in this section. First, an all-glass HAPD was tested with the external readout system and a compact HV supply. Then, the development of the compact readout system and the performance of a complete HAPD is described.

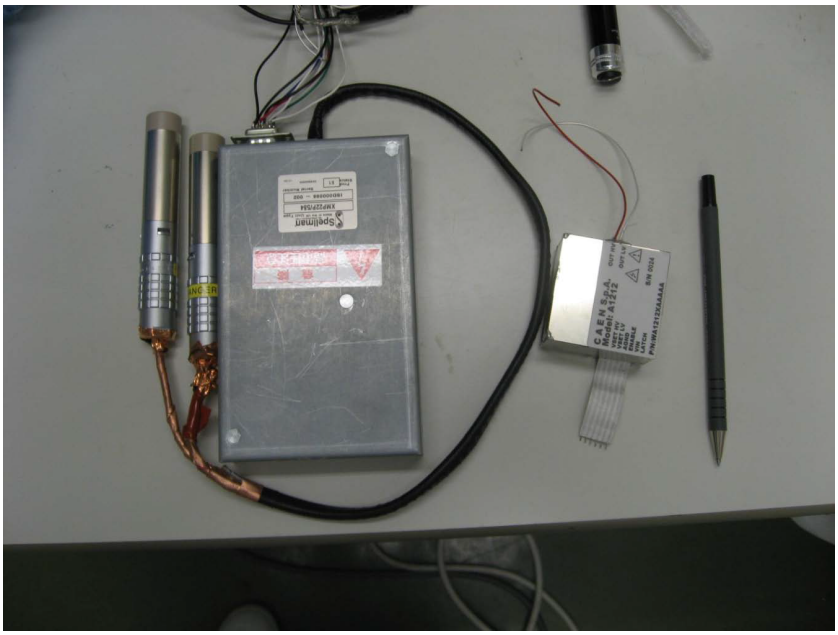

Figure 4.3: Comparison between the HV power supply of the digital HAPD and an ordinary one. The right is the HV system for the digital HAPD.

4.2.1 Performance of all-glass HAPD

A test to evaluate the pulse height and time resolution of the all-glass HAPD is carried out. The setup of the test is the same as shown in Fig. 3.12 except for the HAPD and the HV power supply are renewed. The values of HV and bias voltage are 8 kV and 190 V, respectively.

The raw signal from the analog output of the pre-amplifier is shown in Fig. 4.5. Single and double photoelectron signals are clearly seen.

The pulse height and timing distributions are shown in Fig. 4.6. The single-photon signals are well resolved from the rest and the time resolution is 224 ps. The HAPD made almose entirely of glass supply is proven to work.

4.2.2 Development of a compact readout system

In this subsection, we report on the current performance and future prospects of the readout system.

An overview on the compact readout system

The photographs of the compact readout system are shown in Fig. 4.7. The first and the second layer is on the left and right, respectively. The first layer includes the digital part of the readout system, which is responsible for the

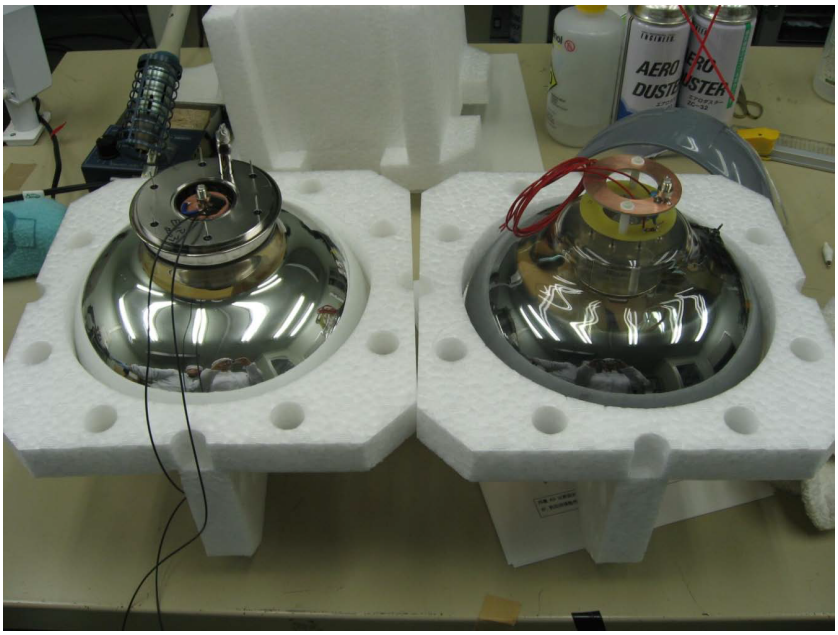

Figure 4.4: Picture of an HAPD with metal flanges (left) and all made of glass (right).

control of the analog part and output of the digital data. The digital part is implemented with FPGA technology. The whole analog part consisting of a pre-amplifier, an AMC and ADCs, is implemented on the second layer of the circuit board. The AMC has 256 cell capacitors and the ADC is driven by a ∼100 MHz clock signal generated in the digital part.

Pedestal level and intrinsic noise of AMC

We measured the pedestal variation and intrinsic noise of the AMC by inputting DC signal generated by a function generator. Note the measurement is performed with the HAPD not connected to the pre-amplifier. The result is shown in Fig. 4.8.

The pedestal variation and intrinsic noise of the AMC are both < 1 mV, while the input width of the waveform sampler is ~ 2V. This means the dynamic range of the waveform sampler reaches 11 bits.

4.3 Performance evaluation of digital HAPD

We conducted a series of test to evaluate the performance of digital HAPDs. The schematic diagram of the setup of the test is shown in Fig. 4.9.

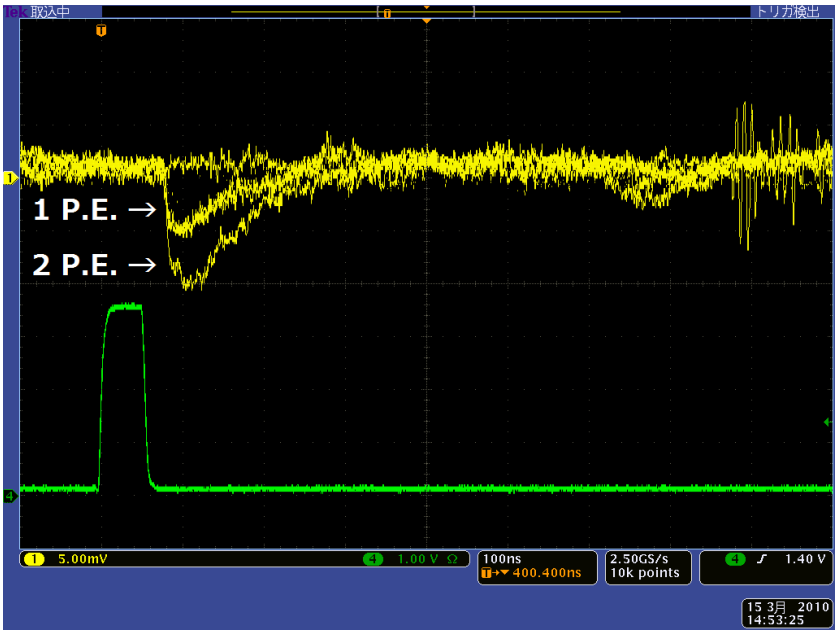

Figure 4.5: The raw signal from the all-glass HAPD.

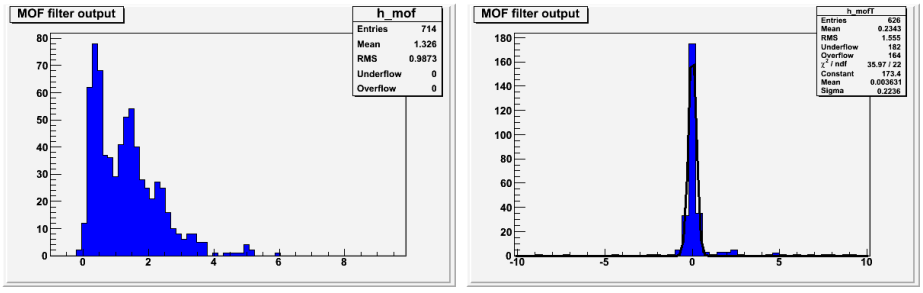

Figure 4.6: Left: Measured pulse height distribution of the all-glass HAPD with the compact HV power supply. The single-photon signal is clearly distinguished from the rest. Right: Measured timing resolution of the all-glass HAPD with the compact HV power supply. The standard deviation is 224 ps.

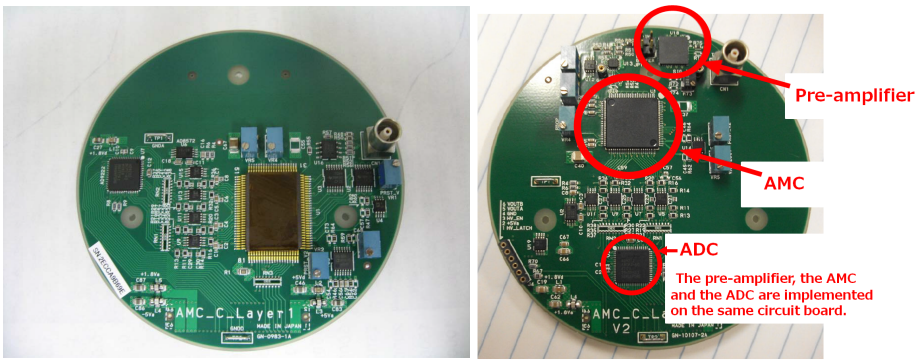

Figure 4.7: Left: The first layer of the readout system including the digital part. Right: The second layer of the readout system including the whole analog part.

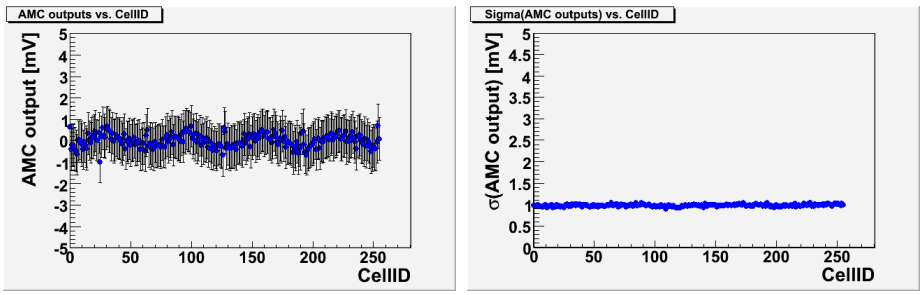

Figure 4.8: Left: AMC output vs. cell number. Right: Intrinsic noise vs. cell number.

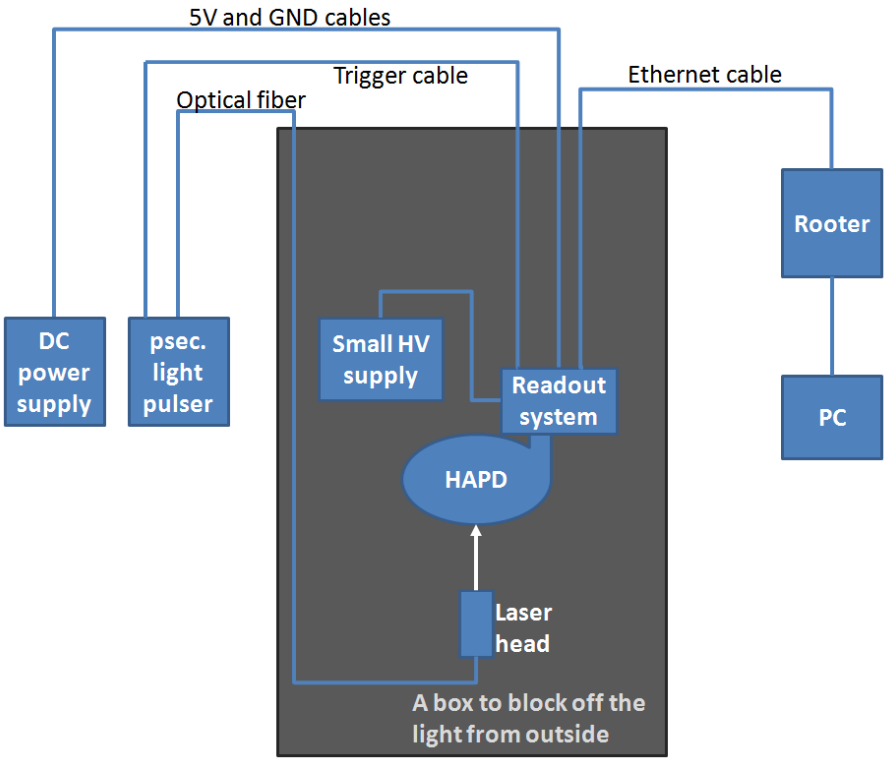

Figure 4.9: The setup of the integration test.

4.3.1 Single photon detection

We describe the single photon detection performance of a digital HAPD in this subsection.

Results before noise suppression

In the beginning of the measurement, the single-photon signal could not be distinguished by using the dedicated readout system for the digital HAPD. However, the single-photon signal was detected by oscilloscope clearly. The comparison of raw signal shapes, noise power distributions and pulse height distributions with the HAPD readout system and the oscilloscope are shown in Fig. 4.10.

We derive the charge and the timing from the peak value and the falling time of the signal shape. The resolution of single-photon signals derived from the output of the oscilloscope is approximately 20%, which means that the analog output from HAPD behaves well if it is not interfered by noises. In order to detect the single photon with the readout system, the noise needed to be significantly reduced.

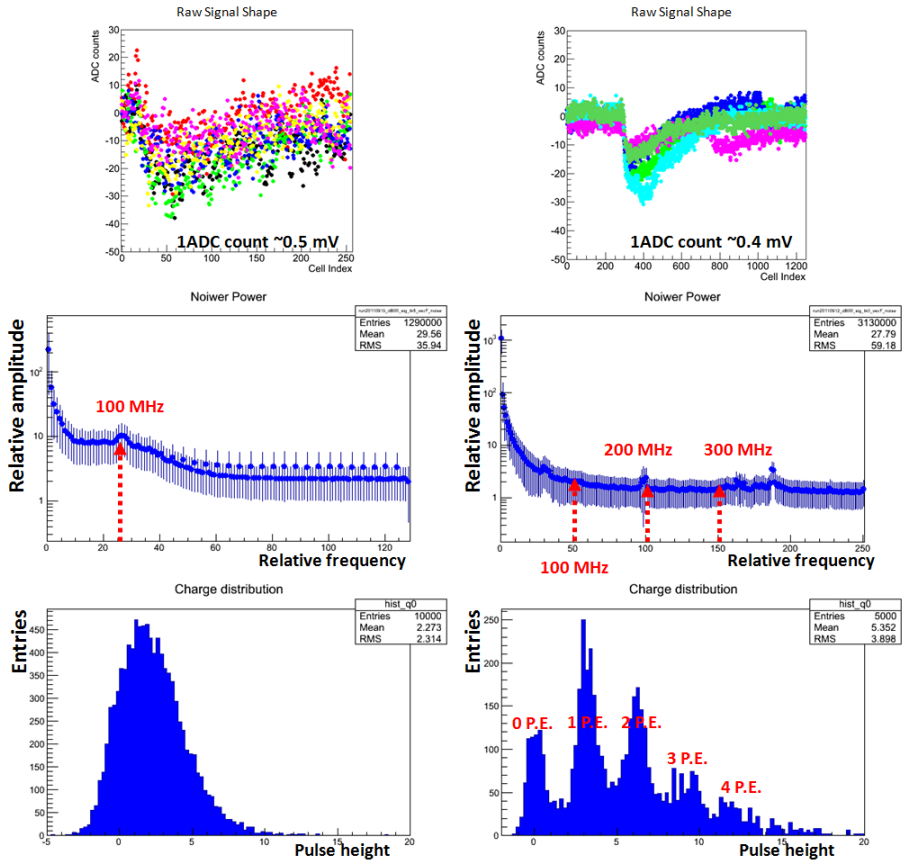

Figure 4.10: Comparison of raw signal shapes (top), noise power distributions (middle) and pulse height distributions (bottom) between the readout system (left) and the oscilloscope (right).

Noise suppression

In order to determine the source of the noises, we measured the intrinsic noise of the output from the waveform sampler with and without the pre-amplifier. The intrinsic noise is measured to be ∼5 mV with the pre-amplifier connected, while it is ∼2.5 mV without the pre-amplifier. This means that noises come from the upstream of the AMC.

We suspect the following as sources of the noise.

- The HV supply and the insulation part of the HAPD.
- The power supply for the pre-amplifier.
- The control signals for the AMC generated in FPGAs in the digital circuit board.

- The clock signal generated in the digital part for digitization of the ADC. The peak appearing in the noise power distribution plot in Fig. 4.10 is due to this clock signal.

In order to suppress noise, we tried the following improvements.

- We have shielded the insulation part of the HAPD with a piece of aluminum foil.
- We have reinforced the ground-level connection between the HAPD and the readout circuit boards with copper tapes.
- We have shielded the wires connecting the HAPD and the readout boards.
- We have changed the bypass capacitor of 0.001 μF to the one of 10 μF.
- We have connected each material with the ground-level.

The pulse height distribution after the above improvements is shown in Fig. 4.11. The single-photon signals are distinguished from the dark counts with the resolution of 29.7 %.

The noise power distribution before and after noise suppression are shown in Fig. 4.12. The distribution after the noise reducing procedure has lower values through all frequency range, and noise suppression is especially effective in the low frequency region.

After much effort on the noise reduction, we have achieved the detection of single-photon signals.

4.3.2 Suggestion for future development

After struggling to suppress noise from the readout system as described above, we have learned how difficult it is to reduce noise coming from a circuit board which has already been produced. The lesson is that we must consider the way to suppress noise seriously when the circuit board is designed.

When we design the next version of electronics, the following points should be taken into account.

- To layout ground plane to a place near the wires through which control signals and clock signals propagate.
- To cover the pre-amplifier with a shield.
- To connect the pre-amplifier with ground-level using wire with appropriate thickness.
- To place a bypass capacitor with adequate capacitance near the pre-amplifier.

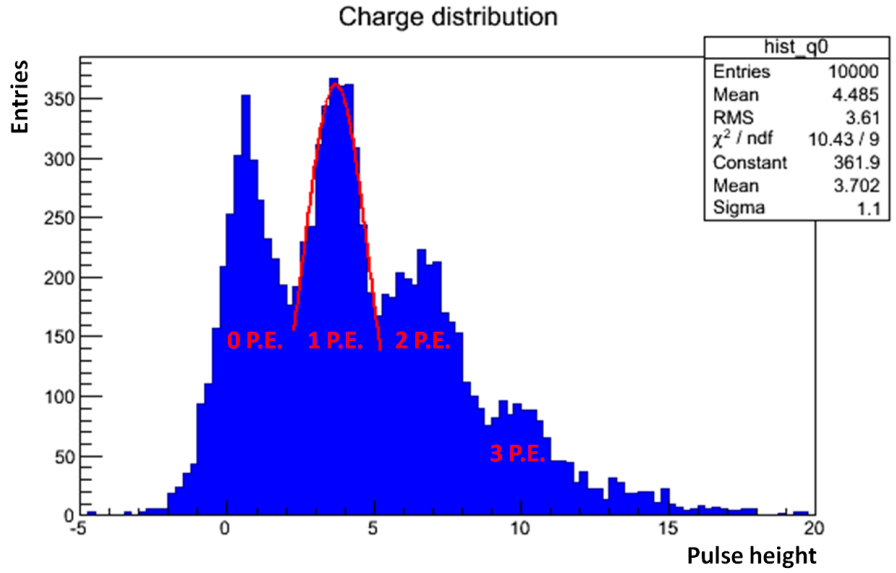

Figure 4.11: Pulse height distribution after noise suppression. The single-photon signals are clearly distinguished.

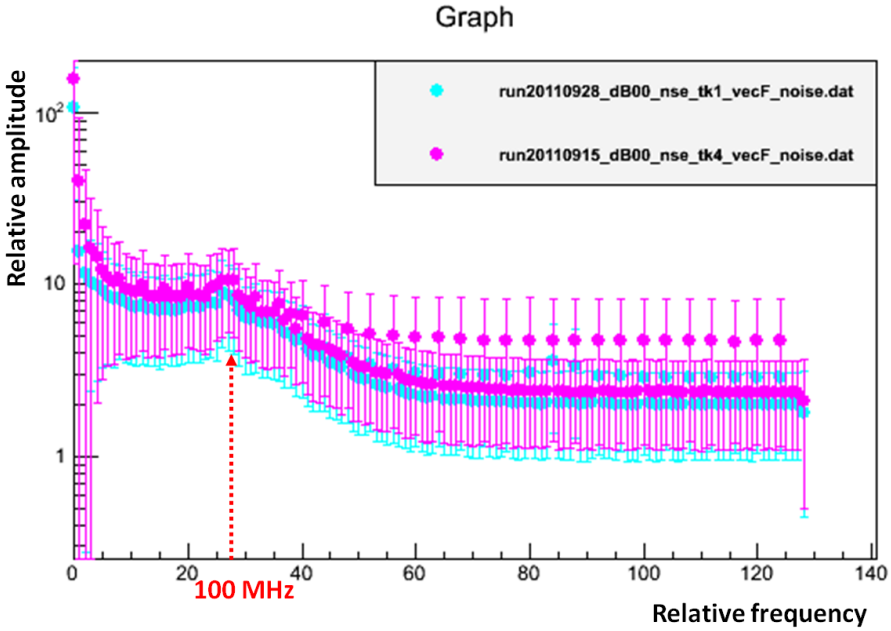

Figure 4.12: Noise power distribution before (magenda) and after (cyan) noise suppression.

Chapter 5

Development of a new readout system for digital HAPD

As seen in the previous chapter, the performance of readout electronics is a key of HAPD development. In order to further improve the performance of the electronics, we have developed a readout system with a waveform sampler consisting of an AMC with ADCs implemented on a monolithic IC. The motivation of this development is to make the system smaller and to reduce power consumption. We have chosen a Wilkinson ADC (WK-ADC) because they have moderate power consumption and simple structure.

In this chapter, we describe the principle of WK-ADC, the implementation of the readout system, and the basic performances of the readout system. The readout system is currently evaluated using an original size board for evaluation, but once completed, it will be implemented on a compact board to be installed in the digital HAPD in future.

5.1 Principle of a WK-ADC

As is shown in Fig. 5.1, a WK-ADC is composed of a pulse stretcher with a capacitor to sample and hold the voltage of input signal, a current source to pull out the charge from the capacitor at a constant rate, a comparator to compare the voltage of input signal with the threshold voltage, and a high-frequency clock with a counter for digitization.

A WK-ADC operates as follows.

1. The pulse stretcher holds the input voltage and electric charge of an amount proportional to the voltage of input signal is stored in the capacitor.

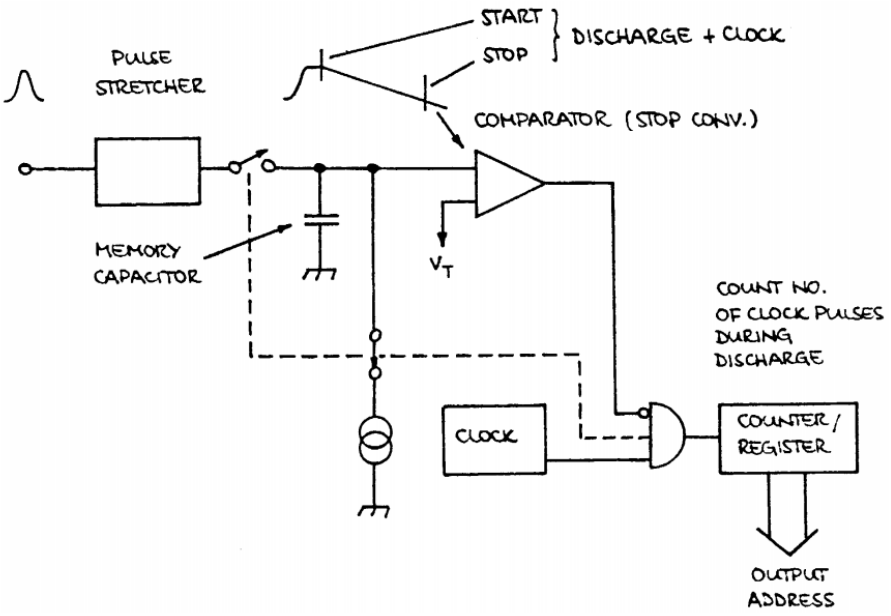

Figure 5.1: Schematic diagram of a Wilkinson ADC [17].

2. As the current source pulls out the charge from the capacitor, the difference between electric potentials of the two electrodes decreases at a constant rate.

3. As soon as the current source starts to pull the charges, the clock and the counter begin to measure the time in a discrete manner.

4. The signal to stop the clock is sent when the potential difference between the two pole plates of the capacitor gets lower than the threshold voltage V_{th}.

Thus, the number of counted clock signals represents the voltage of input signal and digitization is finished. Figure 5.2 shows the timing chart of a WK-ADC.

5.2 Implementation of the readout system

The new readout system has a pre-amplifier, a waveform sampler and a digital part to control the analog part and to transmit digitized data, whose baseline design is the same as the readout system described so far except for the specific implementation.

The waveform sampler is composed of an AMC and WK-ADCs. In order to suppress power consumption and noise, we have implemented an AMC and WK-ADCs on a single piece of IC. However, to prevent high frequency noise which

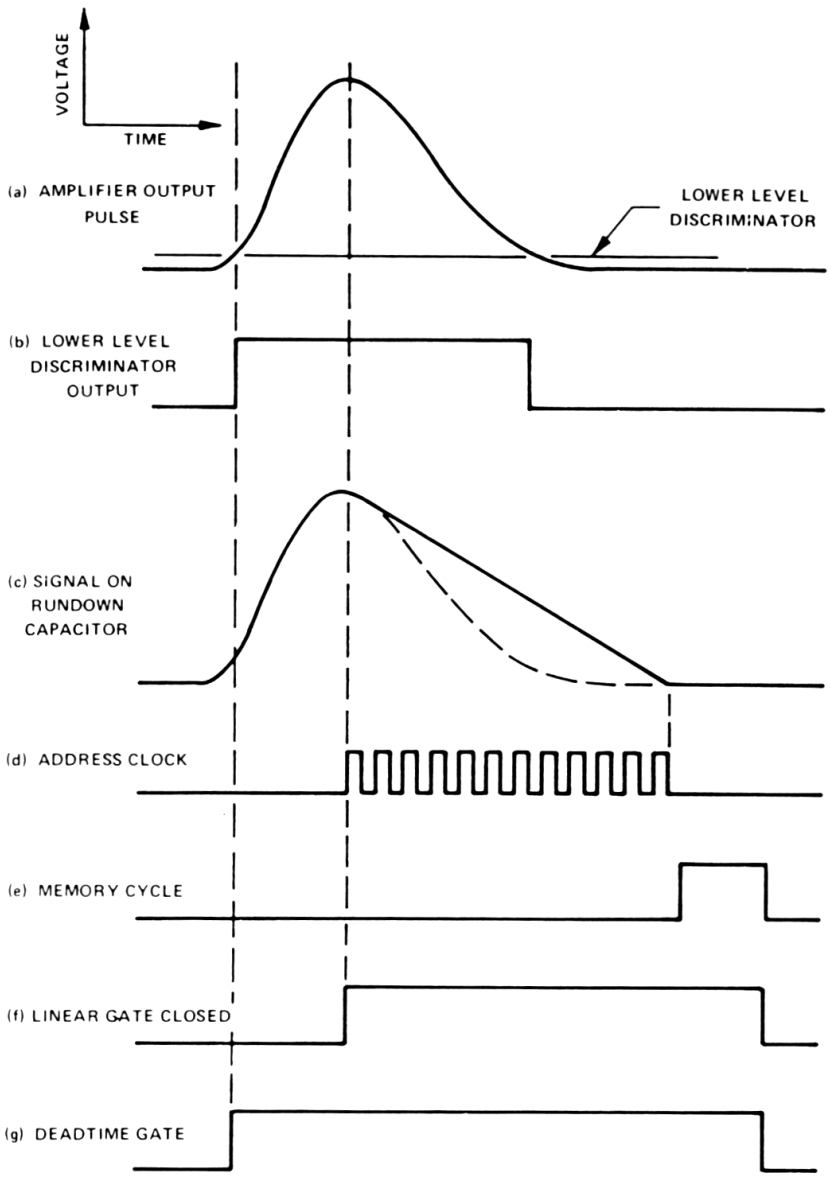

Figure 5.2: The timing chart of a WK-ADC [18].

attributes to the clock signal from the waveform sampler, we implemented the clock and the clock counter with FPGAs which are on the other circuit board. A photograph of the readout system is shown in Fig. 5.3.

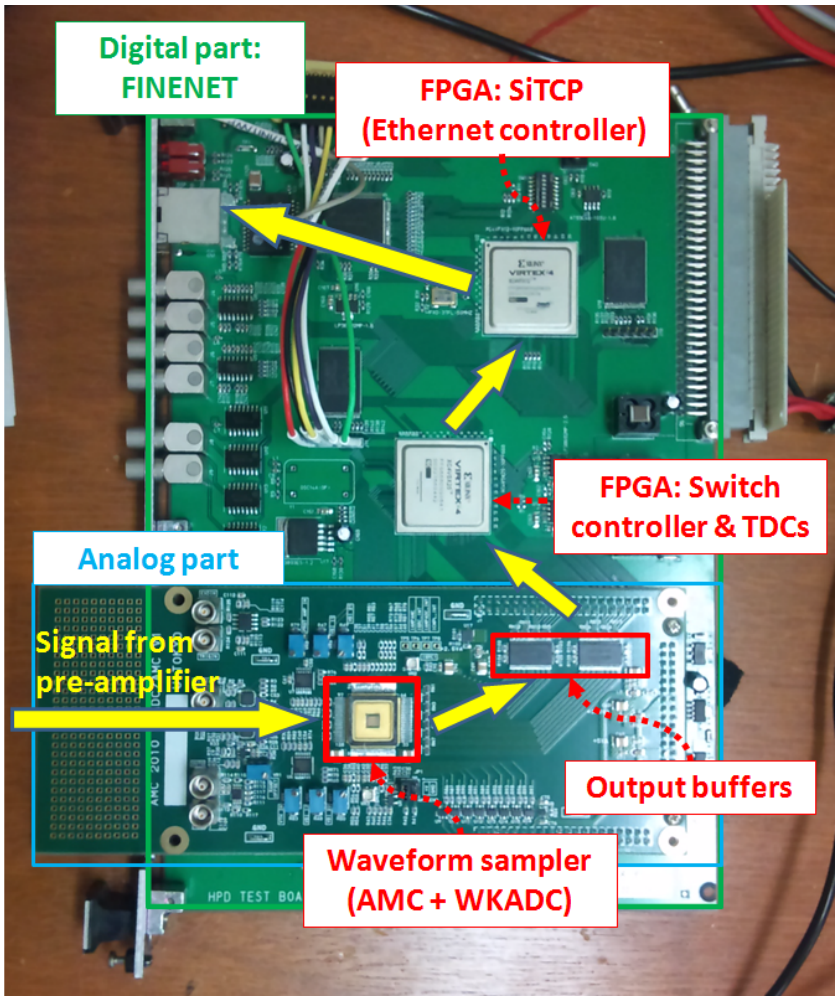

Figure 5.3: A photograph of the readout system.

The AMC in this waveform sampler has 1024 cell capacitors divided into 16 channels. Each of the channels has 32 pairs of cell capacitors operating in a differential mode to reduce common mode noise and has a WK-ADC with two TDCs (see Fig. 5.4). The principle of an AMC is explained in subsection 3.5.2.

If we express the analog output from the j-th cell capacitor in the i-th channel of the waveform sampler by $y_{i,j}$ $(i = 1, \cdots, 16;\ j = 1, \cdots, 32)$, it can be written as follows by using the switching frequency f Hz of the cell capacitors.

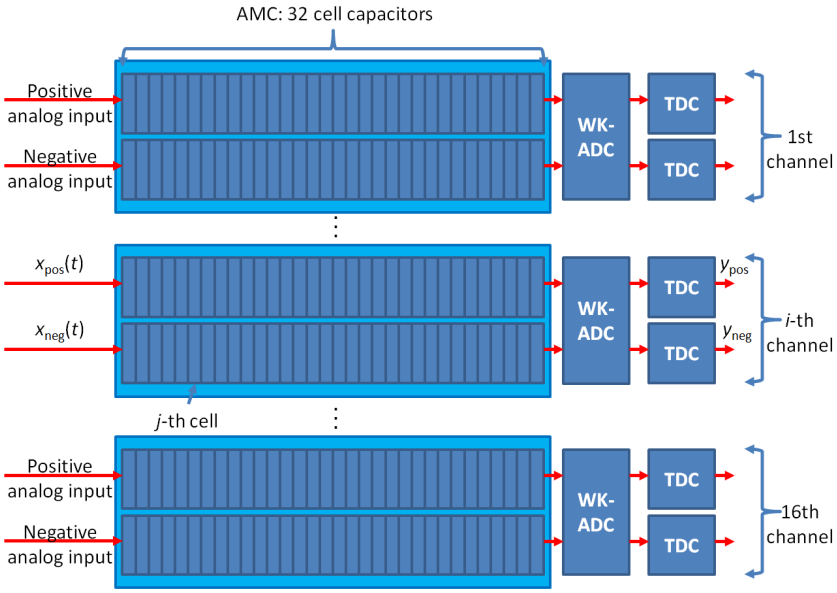

Figure 5.4: The schematic diagram of the waveform sampler.

$$y_{i,j} = H\left[x\left(\frac{1}{f}\left(32\left(i-1\right)+j\right)\right)\right], \tag{5.2.1}$$

where $x\left(t\right)$ and $H\left[\cdot\right]$ represent the analog input to the AMC and the effect of the waveform sampler on the inputs, respectively. The analog output represents the voltage of the input signal in discrete time domain.

Since we record a large number of events when we take data, we use the notation $y_{i,j}^{k}$ $(k = 1, \cdots, N_{\text{events}})$, where N_{events} is the number of recorded events, to represents the digitized final raw output of k-th event. We define the mean value over events and the mean value over cells in the j-th channel as

$$\begin{cases} \text{Mean value over events:} \\ \qquad \overline{y_{i,j}} := \dfrac{1}{N_{\text{events}}} \displaystyle\sum_{k=1}^{N_{\text{events}}} y_{i,j}^{k}\,, \\ \text{Mean value over cells in the } i\text{-th channel:} \\ \qquad \langle y_i \rangle := \dfrac{1}{32} \displaystyle\sum_{j=1}^{32} \overline{y_{i,j}}\,. \end{cases} \tag{5.2.2}$$

5.3 Performance evaluation

We describe the basic performance of the new readout system in this section. First, we show the raw output from the AMC and WK-ADC to give an overall

picture of the system. Second, we explain the calibration process with respect to $\langle y_i \rangle$ and $\overline{y_{i,j}}$, respectively. Third, we show the results of linearity evaluation and AC response evaluation. Finally, we discuss the performance and propose a future plan of development.

5.3.1 Raw outputs from the waveform sampler

A couple of raw outputs from the waveform sampler are shown in Fig. 5.5. The top one is for an input with low DC voltage, while the bottom one is for an input with high DC voltage. The positive width of the output pulse from the analog part of the WK-ADC is proportional to the pulse height of the analog outputs from AMC. The pulse width of the output from the analog part of the WK-ADC is digitized in a TDC with a clock and a clock counter.

5.3.2 Calibration

As is shown in Fig. 5.6, the digitized raw output from TDCs have large dispersion from one channel to the other despite the input signal being DC voltage. Hence, we have carried out offline calibration on the digitized outputs.

We explain two types of calibration we have performed in this subsection: 1) calibration on each channel and 2) calibration on each cell.

Calibration on each channel

We have performed a series of calibrations to compensate the large differences among channels, by using the mean value over the 32 cells in each specific channel $\langle y_i \rangle$ ($i = 1, \cdots, 32$).

The full procedure of the calibration is explained below.

1. We calculate the mean value $\langle y_i \rangle$ in each channel and draw a gain curve with respect to the voltage of input signals.
2. We fit all gain curves with linear functions in a specific range. This range for fitting is determined to let the linearity performance be the best.
3. We set the offsets of the gain curves at the input DC voltage of 1.26 V to 0.
4. We correct the shape of each gain curve by a conversion factor which is derived from the fitting function.

The effects of calibration on the gain curves are shown in Fig. 5.7, 5.8 and 5.9.

As can be seen from the Fig. 5.9, although the large dispersion among channels are almost eliminated, there still exist non-negligible differences because each channel has a different non-linearity response. We will come to this later in the subsection 5.3.3, in which we discuss linearity evaluation.

Besides this, there is non-negligible dispersion of ~ 3 mV even among the cells belonging to the same channel (see Fig. 5.8). This is why calibration for each cell is needed.

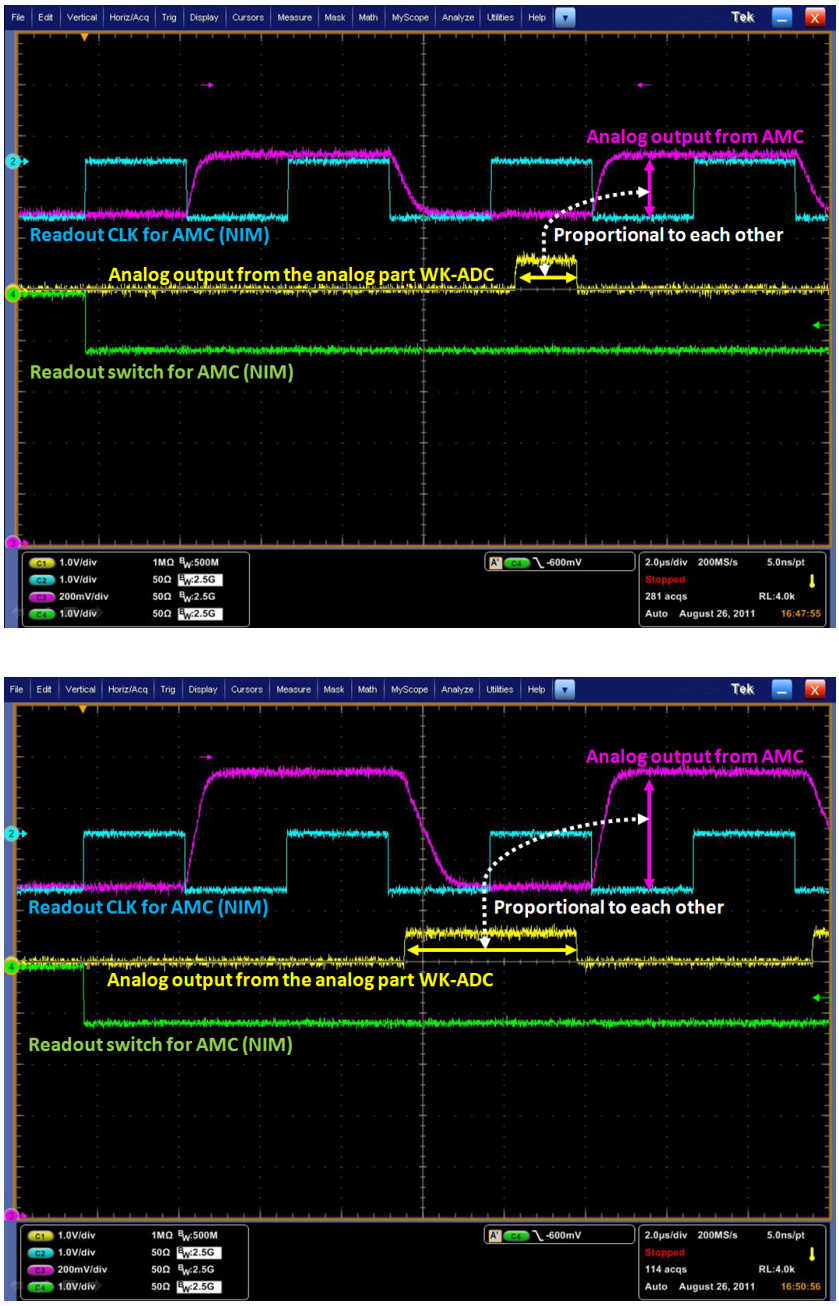

Figure 5.5: Raw outputs from the waveform sampler.

Calibration on each cell

We calibrated the raw digital data $y_{i,j}$ with respect to each cell. The way we have done the calibration is almost the same as those in the previous subsubsection,

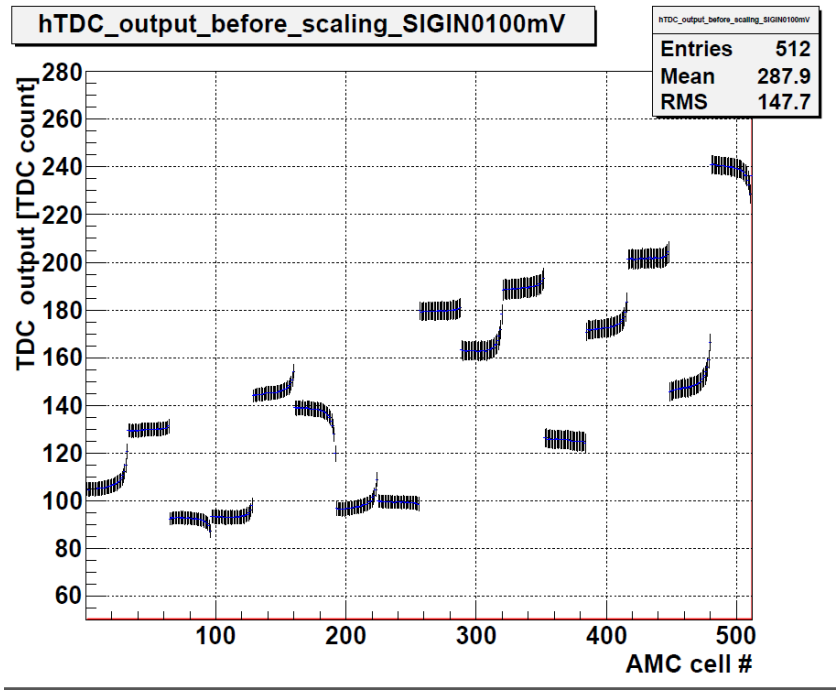

Figure 5.6: The output from TDC without any calibration. The little blue markers and error bars represent mean values and standard deviations of output from each cell over 990 recorded events, respectively. The DC voltage of input signal to AMC is 1.2756V in this figure.

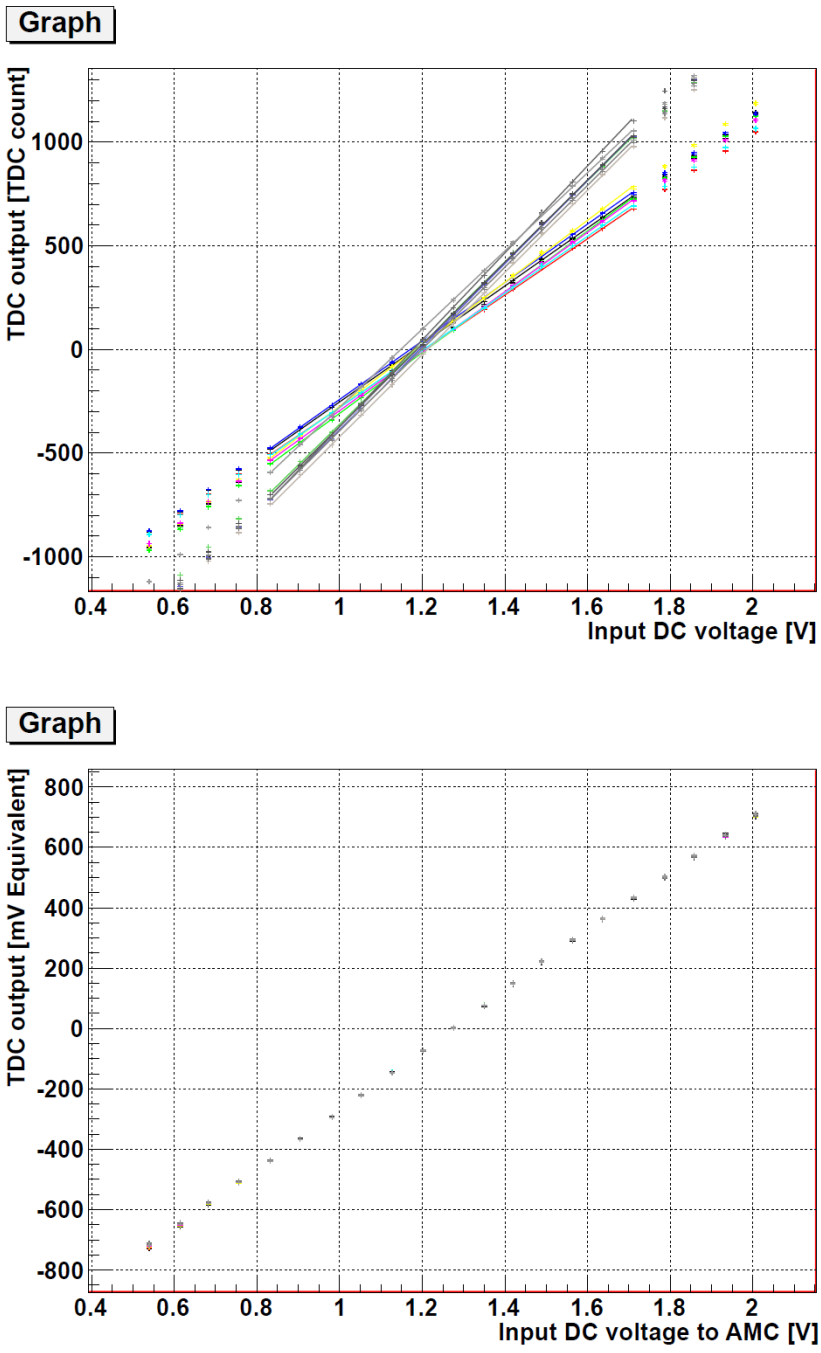

Figure 5.7: Comparison of gain curves before/after calibration on channels. The top is the gain curve before and bottom after calibration on channels, respectively. The difference in color represents different channels. The fitting range is set to be 0.8323 -1.7118 V.

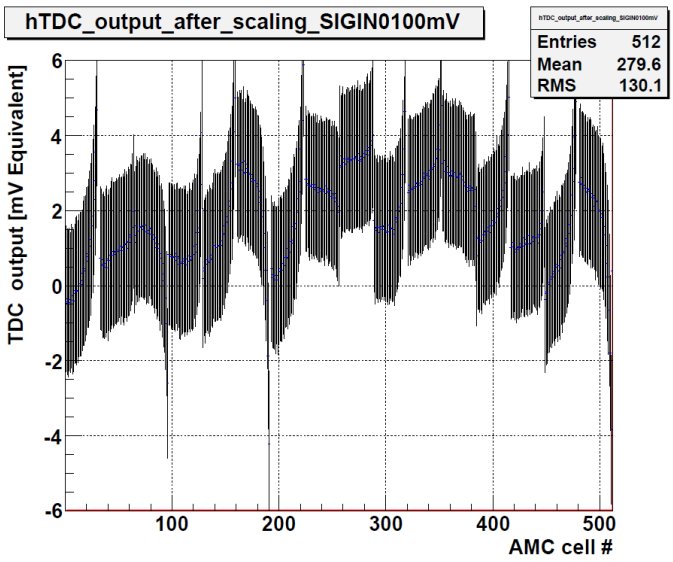

Figure 5.8: The TDC output calibrated with respect to the gain curves made from mean values in each channel. The little blue markers and error bars represent mean values and standard deviations of output from each cell over 990 recorded events in mV equivalent unit, respectively. The DC voltage of input signal to AMC is 1.2756V. Compare this Figure with Fig. 5.6.

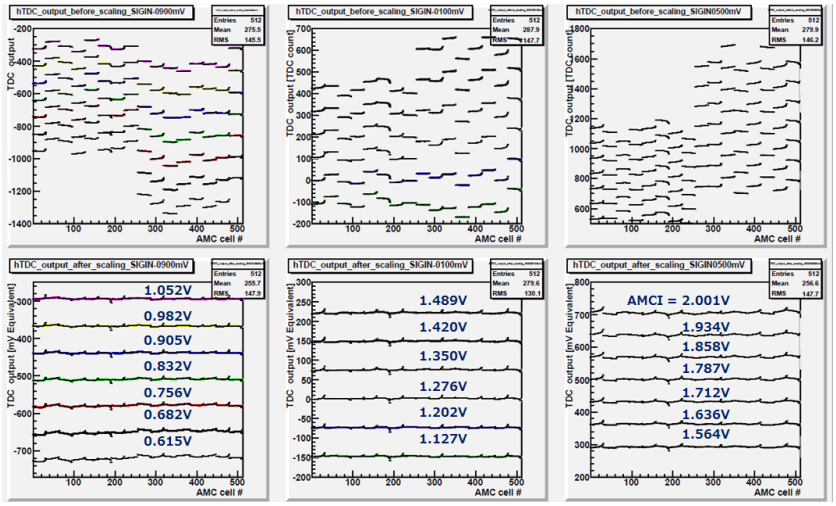

Figure 5.9: Comparison of TDC output before/after calibration on channels. The top is the digital output from TDC before and bottom after calibration on channels, respectively. The difference in colors represents different input DC voltage to AMC.

except that we have substituted the mean value for each of the cells over events $\overline{y_{i,j}}$ for the mean value over cells belonging to the same channel $\langle y_i \rangle$ in the first step, hence we have made 512 gain curves and followed the same procedure explained above to carry out calibration.

One of the results of the calibration is shown in Fig 5.10.

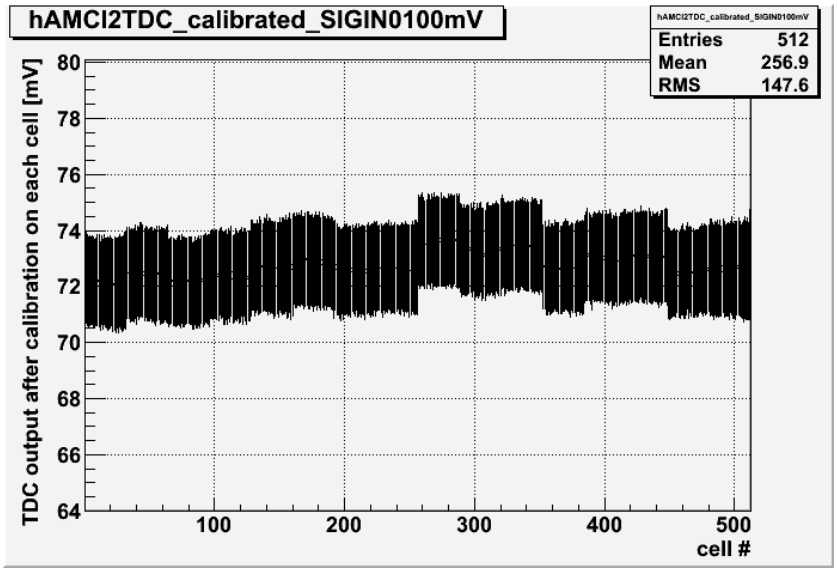

Figure 5.10: TDC output after calibration with respect to gain curves of all 512 cells. he DC voltage of input signal to AMC is 1.2756V. Compare this Figure with Fig. 5.8.

The dispersions between cells belonging to the same channel have been eliminated, and the differences still existing are due to the disparities in non-linearity of each channel.

Since the range of fitting is 0.8323-1.7118 V, the intrinsic noise of <2 mV and the dispersion of pedestal of <1.5 mV give the resolution of 8.8 bits and 9.2 bits, respectively. These values are lower by approximately a bit than the design value of 10 bits. The analog output of the AMC is responsible for this because it is the origin of the intrinsic noise of ∼2 mV. If we can reduce the intrinsic noise of the AMC to sub-mV level, the resolution will meet the design value.

5.3.3 Linearity evaluation

We evaluated the linearity of the new waveform sampler, including TDCs, by measuring its output responses to various values of input DC voltage. In this subsection, we describe the results of the linearity evaluation.

Linearity of analog output from AMC

We show the evaluated linearity of analog output from AMC in Fig. 5.11 by presenting the residual from linear approximations and linearity in bit with respect to Integral Non-linearity Errors (INE). Linearity in bit with respect to INE is defined as follows.

$$\text{(Linearity in bit with respect to INE)} := \log_2 \frac{\text{(Fitting range)}}{\text{(Maximal residual)}} \tag{5.3.1}$$

The linearity was measured to be 7.64 with respect to INE.

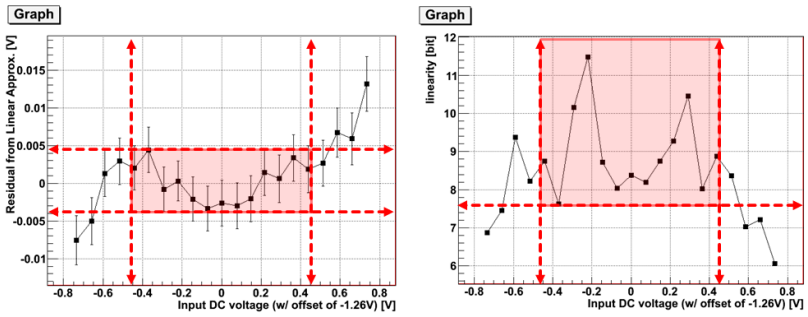

Figure 5.11: The linearity of analog output from AMC after calibration.

Linearity of the analog part of WK-ADC

The linearity of Wilkinson ADCs (with TDCs) itself is displayed in Fig. 5.12. They have only 6.6±0.3 bits of linearity with respect to INE. This is not satisfactory compared to the design value of 11 bits and we will come back later on this point.

Linearity of TDC

The linearity of TDC implemented with FPGA in the digital circuit of the system has been measured to be better than 13 bit with respect to INE. This indicates that the TDCs do not spoil the linearity of the system at all.

Linearity of the whole waveform sampler

The results of linearity analysis for the whole system of the waveform sampler, i.e. AMC and WK-ADCs with TDCs, are shown in Fig. 5.13. We show the plots after calibration on channels since it is not convenient to select plots out of 512 for calibration on cells. The whole system has been proven to have 7.11±0.07 bit of linearity with respect to INE. This value is calculated by applying calibration on each cell.

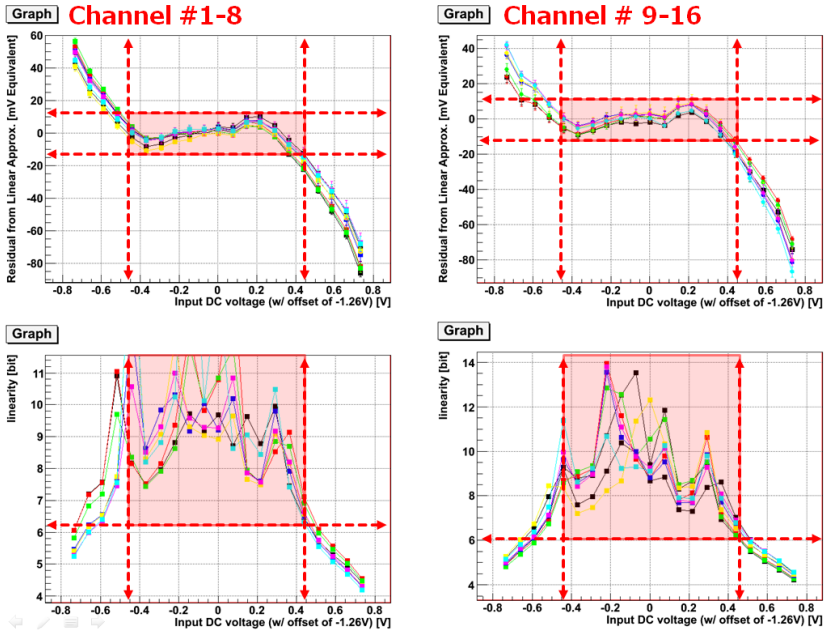

Figure 5.12: The Linearity plot of the Wilkinson ADC. The above ones show residuals from linear approximation of gain curves calibrated with respect to each channel and the bottom ones show the linearity in bit with respect to INE.

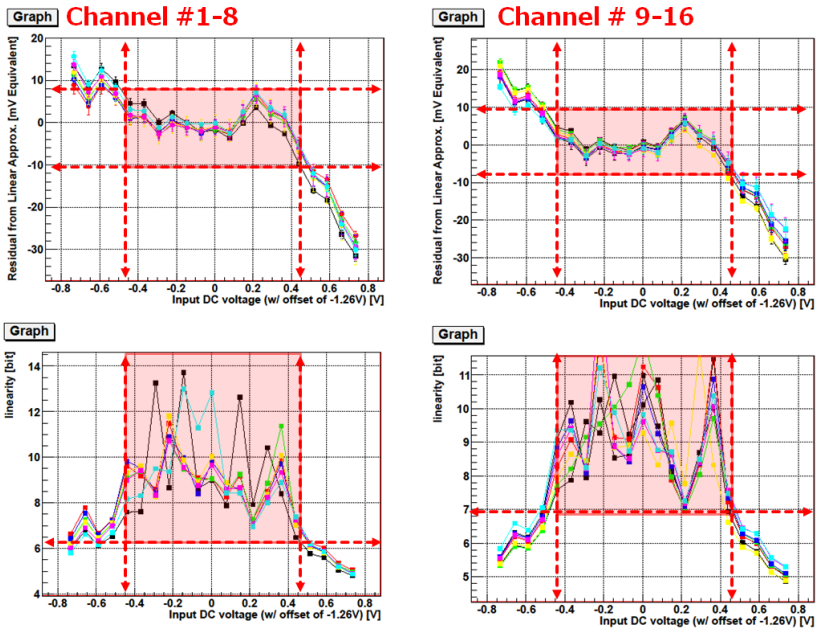

Figure 5.13: The linearity plot of the whole system. The above ones show residuals from linear approximation of gain curves calibrated with respect to each channel and the bottom ones show the linearity in bit with respect to INE.

Discussion

The overall linearity of our new waveform sampler is approximately 7.1 bits with respect to INE, which is not satisfactory compared to the design value of 10 bits. The WK-ADC is mostly responsible for this. The reason is that we use a larger current of $\sim$20 μA, than the ordinary value of a few μA, to pull out electric charge of the memory capacitor to suppress noise and to compensate the operation speed. In principle, the noise (jitter) of an WK-ADC is inversely proportional to the value of the current draw, and it is not realistic for us to lower our pulling current than 20 μA by a large value regarding the noise of $\sim$2 mV in our case. The non-linearity of the source of pulling currents can also be responsible for the non-linearity. In any case, however, once detailed gain curves for all of the cells are obtained, it will be possible to carry out calibration to compensate the non-linearity. The AMC does not reach the linearity of design value either. The reason could be the difference in the values of cell capacitors.

It is important to search for the true cause and solution of the non-linearity, and at the same time suppression of noise is equally crucial as a task of future R&D work.

5.3.4 AC response evaluation

We describe the measurement and evaluation of AC response of the waveform sampler in this subsection. We have used a pulse generator to produce AC signals with amplitude of 300 mV and various frequencies between 20 MHz and 500 MHz. Since the sampling rate of the waveform sampler is designed to be $\sim$1 GHz, it is not possible to reconstruct input signals whose frequency is higher than 500 MHz due to aliasing.

The raw digitized output from the waveform sampler with 160 MHz input, the waveform after calibration on each cells, and the Fast Fourier Transformation (FFT) of the waveform after calibration on each cells are shown in Fig. 5.14. We have not applied any recalibration to compensate linearity in this study.

The results of analog bandwidth analysis and frequency reconstruction are shown in Fig. 5.15. We defined the amplitude $A_{\rm rec}$ and frequency $f_{\rm rec}$ reconstructed from the waveforms after calibration as the maximal value of the FFT magnitude and the frequency giving the maximal value, respectively (see the bottom plot in Fig. 5.14). We adopt the standard deviation of the Gaussian fitting to the FFT magnitude as errors for frequency reconstruction. The relative gain $A_{\rm rel}$ at input frequency of f MHz is defined as

$$A_{\rm rel}\left(f\right) := 20\log_{10}\frac{A_{\rm rec}\left(f\right)}{A_{\rm rec}\left(20\right)} \quad [\text{dB}] \tag{5.3.2}$$

where $A_{\rm rec}\left(f\right)$ is the reconstructed amplitude at input frequency of f MHz.

Bandwidth of relative gain drop of 3 dB is 0-150 MHz and this is good enough for us to handle pulse signals with rising time of several nano-seconds, where relative gain drop of 3 dB corresponds to factor 0.71. The sampling frequency of

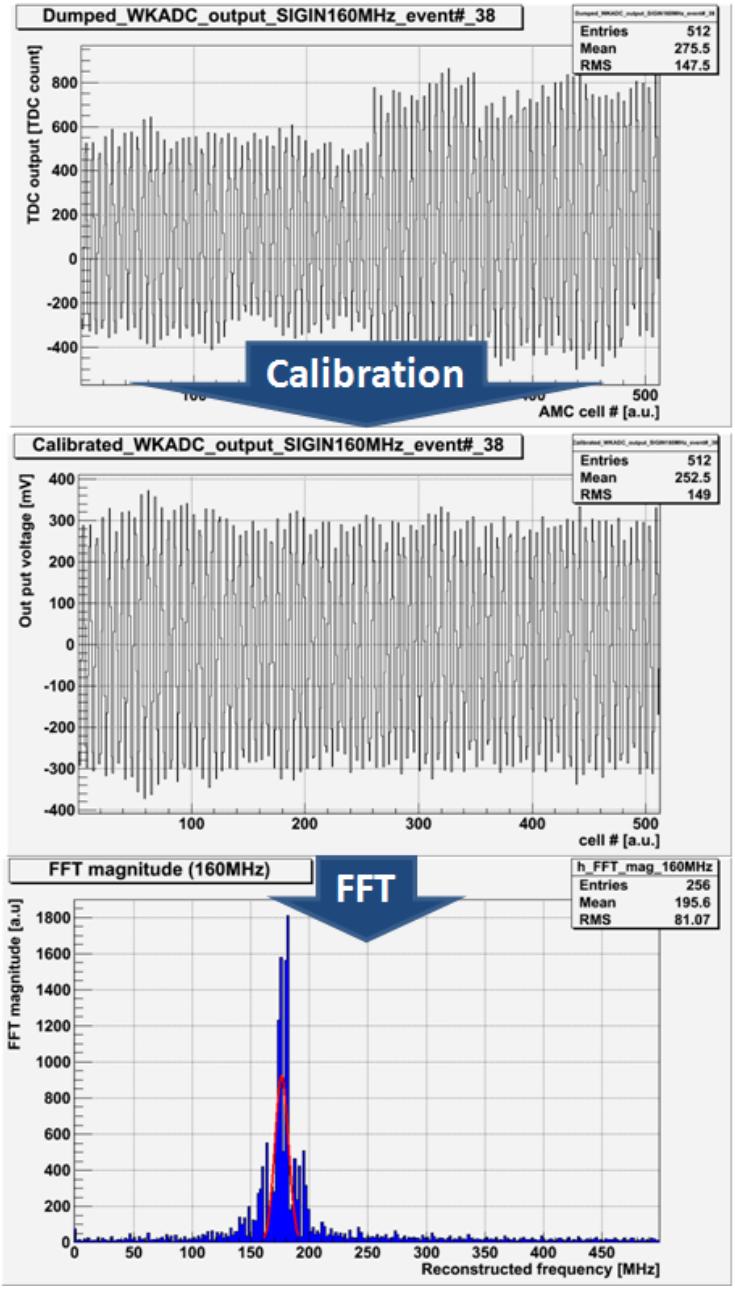

Figure 5.14: The top, middle, and the bottom plot show raw data output from TDC, data calibrated on each cell and Fast Fourier Transform (FFT) of the calibrated data, respectively.

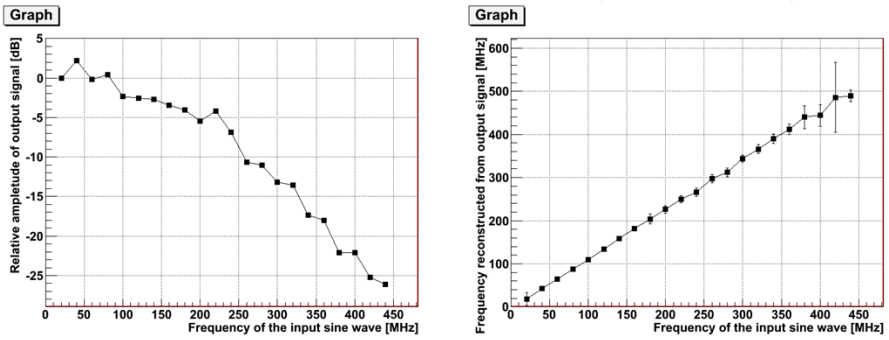

Figure 5.15: Left: Relative amplitude as a function of input frequency. Right: Reconstructed frequency as a function of input frequency (The sampling frequency of our waveform sampler is assumed to be 1 GHz).

the AMC in our waveform sampler is calculated to be ∼875 MHz, which is lower than the design value of 1 GHz. With sampling rate of 1 GHz, the AC response may be better. The effect of this should be studied in the future. The frequency reconstruction goes with reasonable resolution upto ∼350 MHz, which means that a signal with frequency below 350 MHz is possible to be resolved if noise is low enough.

Summary

We have evaluated basic performances of the developed readout system.

The resolution of the waveform sampler is 8.8 bits, which is lower by about a bit than design value. Noise suppression for the AMC is essential to improve this. The linearity of the system is 7.11 bits, which is lower than design value of 10 bits by approximately 3 bits. The most responsible for the large non-linearity is the analog part of WK-ADC. However, if the noise is reduced to sub-mV level to meet the requirement, we can lower the current draw, which will help us improve linearity.

The AC response of the system is satisfactory to capture pulse signals whose rising time is a few nanosecond although the sampling rate is lower by 125 MHz than the requirements.

Chapter 6

Summary

A new photosensor, the Hybrid Avalanche Photo-Detector (HAPD) and its dedicated readout system have been developed for next generation water Cherenkov detectors.

A package of an HAPD, HV power supply and the readout system, aiming at cost reduction and improvement in user-friendliness, has been developed. The performance of this package, the "digital HAPD," has been confirmed to be able to detect single-photon signals successfully. In addition, the new HAPD uses a glass structure instead of metal flanges in order to simplify the structure and reduce cost. The new design has been proved to have the same performance as the old ones.

R&D work of a readout system for improved performance has been carried out. A new prototype waveform sampler with Wilkinson ADCs was measured to have $\sim$7-bit resolution in linearity, which can be improved with calibration along with the gain curves, and analog bandwidth of $\sim$150 MHz. This is the first attempt to develop such electronics with AMC and ADCs implemented in a monolithic IC. We have confirmed basic functionality of the readout system and identified several issues that need to be resolved. After further R&D, the electronics will be used in digital HAPDs in future.

Appendix A

Development of a dead time less readout system

Detection of neutrinos emitted from supernovae is one of the most important missions for next generation water Cherenkov detectors. In case of a supernova happening in a very short distance to the earth, the readout system is forced to work at a very high rate not to lose any information of the precious supernova neutrino events.

In order to meet this needs, we have been developing a dead time less readout system for the digital HAPD. We report current status of our R&D work.

A.1 Overview of the system

At first, we plan to realize a dead time less readout system with a waveform sampler operating at 1 GHz. The schematic diagram is shown in Fig. A.1.

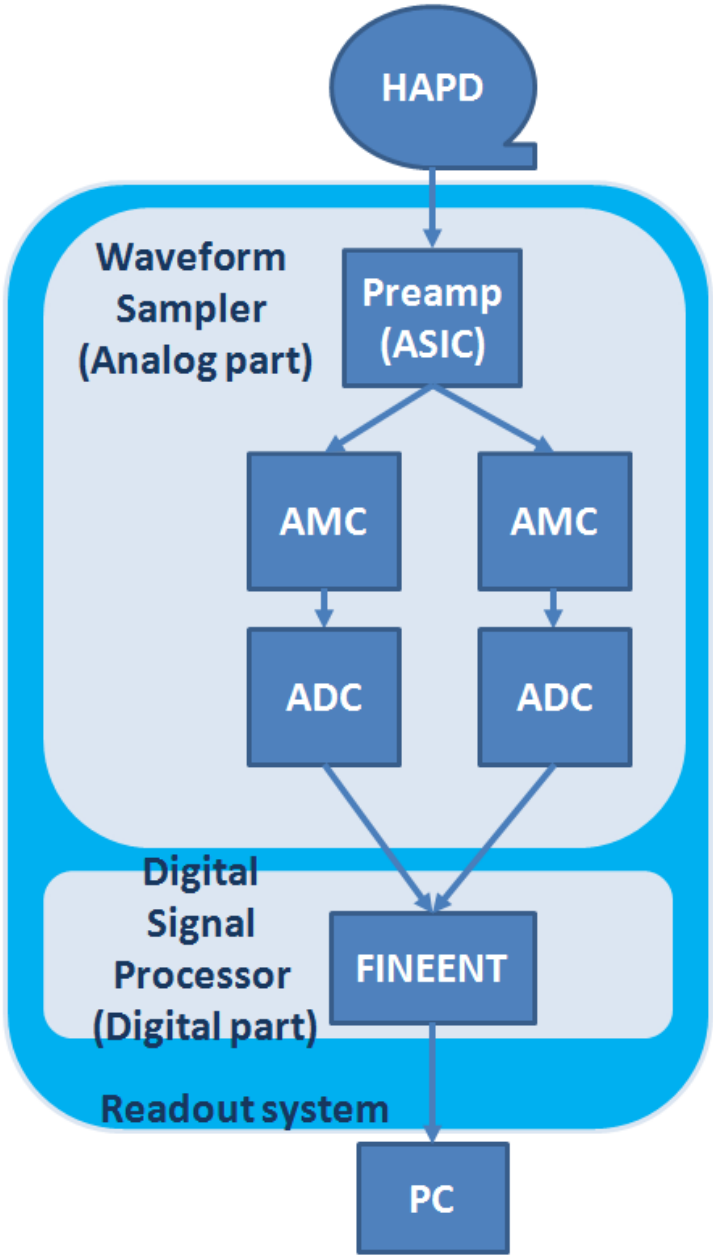

Figure A.1: Schematic diagram of dead time less readout system.

The waveform sampler has a couple of AMC with ADC parallel to each other operating complementarily. Driven at a rate of 1 GHz, the 1024 cell capacitors in one AMC of the two can cover $\sim$1 μs as a data buffer. While the ADC connected to this AMC is digitizing data, the other AMC records the input voltage as a data buffer, which enables us to readout the data without dead time[1].

In order to realize this readout system, an ADC with 1) resolution better than 11 Effective Number Of Bits (ENOB) and 2) operation frequency larger than 1 GHz is indispensable. An pipeline ADC attempted to meet these two demands has been under development.

We describe the performance evaluation of proposed pipeline ADC using circuit simulation in this section.

A.2 Performance evaluation of pipeline ADC

The pipeline ADC is designed to be driven with a 100 MHz clock signal and our plan is to allocate more than 10 of them with multiplexer to achieve the operation rate faster than 1 GHz. The simulated output corresponding to the input alternating current signal with 300 mV amplitude and 9.766 MHz frequency is shown in Fig. A.2.

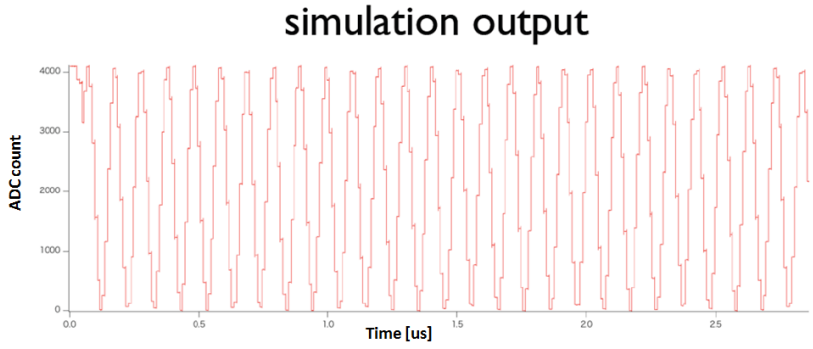

Figure A.2: A simulated output of the pipeline ADC.

Figure A.3 shows the result of FFT of output simulated with different conditions of circuit temperature. According to the simulation, the performance of our pipeline ADC meets the demands well. The summary is on Table A.1

[1]Actually, the ADC must digitize the 1024 pieces of data in $\sim$1 μs, which means that the ADC must operate at 1 GHz after all and seems to leads to a conclusion that the parallel structure of the waveform sampler, or even the AMC, is useless. However, the existence of AMCs plays an important role in widening the analog bandwidth and the parallel structure is to reduce the complexity of switching control.

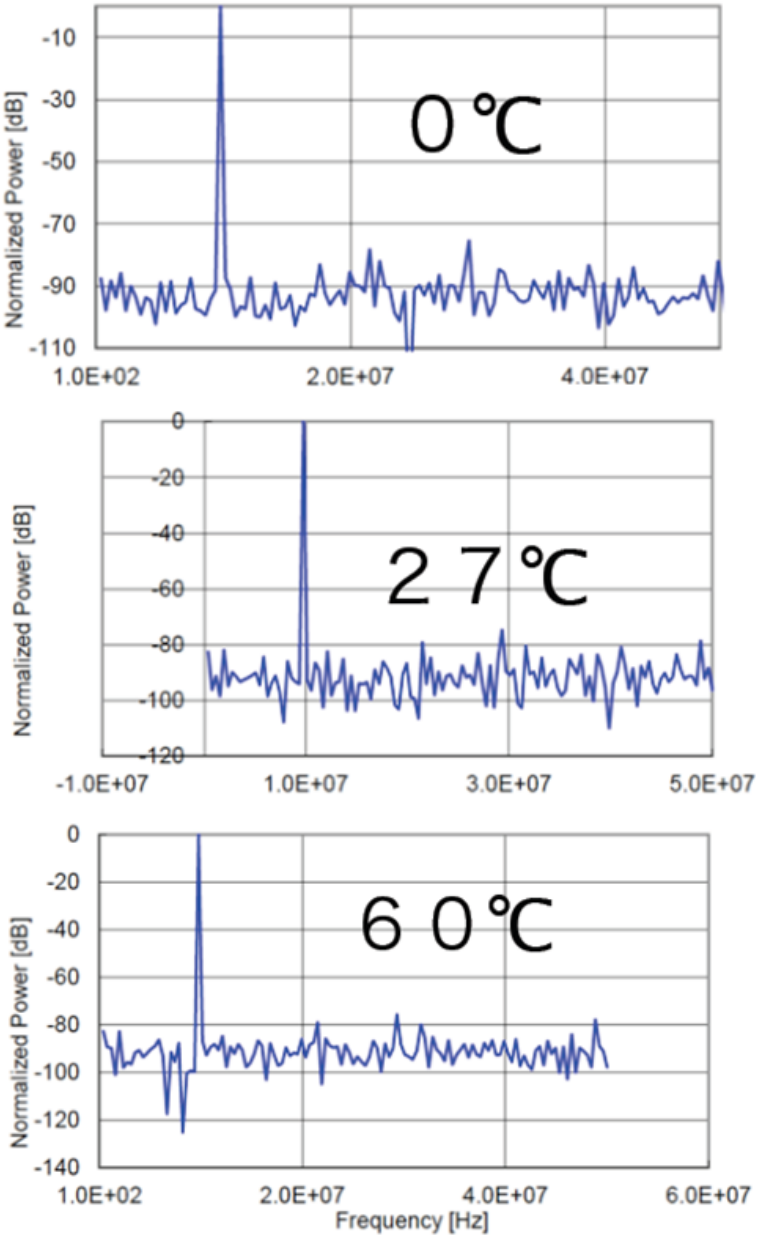

Figure A.3: The FFT of ADC output simulated at 273 K, 300 K and 333 K.

Table A.1: Evaluated performance of proposed pipeline ADC. SNR: Signal to Noise Ratio. ENOB: Effective Number Of Bit.

Parameters	273 K	300 K	333 K
SNR	69.64	68.61	68.88
ENOB	11.03	10.81	10.87

Acknowledgements

I would love to express my great gratitude to my supervisor, Professor Hiroaki Aihara, for his overall supervision. I am deeply indebted to Toshinori Abe, Manobu Tanaka, Yoshihiko Kawai, and the members of the KEK electronics group for their enormous support leading me through new territory. I sincerely appreciate the generous guidance, meticulous feedback and encouragement offered by Masashi Yokoyama. My thanks also goes to Masako Iwasaki, Hidekazu Kakuno, Hiroyuki Nakayama, Denis A. Epifanov, Hironao Miyatake, Hiroki Fujimori, Sogo Mineo, Clement Ng, Shinya Sugihara and Yasutaka Kanazawa for helping me in so many aspects that I cannot even list them up.

Most of all, I would love to express my sincere appreciation to dedication of my parents and my friend Anna Suganuma.

Bibliography

[1] Y. Fukuda *et al.* [Super-Kamiokande Collaboration], "Evidence for oscillation of atmospheric neutrinos," Phys. Rev. Lett. **81**, 1562 (1998) [hep-ex/9807003].

[2] E. Aliu *et al.* [K2K Collaboration], "Evidence for muon neutrino oscillation in an accelerator-based experiment," Phys. Rev. Lett. **94**, 081802 (2005) [hep-ex/0411038].

[3] S. Fukuda *et al.* [Super-Kamiokande Collaboration], "Determination of solar neutrino oscillation parameters using 1496 days of Super-Kamiokande I data," Phys. Lett. B **539**, 179 (2002) [hep-ex/0205075].

[4] M. Nakahata [Super-Kamiokande Collaboration], "Super-Kamiokande's solar neutrino results," Nucl. Phys. Proc. Suppl. **143**, 13 (2005).

[5] Q. R. Ahmad *et al.* [SNO Collaboration], "Direct evidence for neutrino flavor transformation from neutral current interactions in the Sudbury Neutrino Observatory," Phys. Rev. Lett. **89**, 011301 (2002) [nucl-ex/0204008].

[6] K. Eguchi *et al.* [KamLAND Collaboration], "First results from KamLAND: Evidence for reactor anti-neutrino disappearance," Phys. Rev. Lett. **90**, 021802 (2003) [hep-ex/0212021].

[7] T. Araki *et al.* [KamLAND Collaboration], "Measurement of neutrino oscillation with KamLAND: Evidence of spectral distortion," Phys. Rev. Lett. **94**, 081801 (2005) [hep-ex/0406035].

[8] K. Abe, T. Abe, H. Aihara, Y. Fukuda, Y. Hayato, K. Huang, A. K. Ichikawa and M. Ikeda *et al.*, "Letter of Intent: The Hyper-Kamiokande Experiment — Detector Design and Physics Potential —," arXiv:1109.3262 [hep-ex].

[9] B. Pontecorvo, "Neutrino Experiments and the Problem of Conservation of Leptonic Charge," Sov. Phys. JETP **26**, 984 (1968) [Zh. Eksp. Teor. Fiz. **53**, 1717 (1967)].

[10] Z. Maki, M. Nakagawa and S. Sakata, "Remarks on the unified model of elementary particles," Prog. Theor. Phys. **28**, 870 (1962).

[11] F. A. White, J. C. Sheffield, "Reversed-biased P-N junctions in electron tubes," Proc. I.R.E. **50**, 1523 (1963).

[12] R. DeSalvo, "Hybrid Photodiode Tube," CLNS-87-92.

[13] A. Kusaka, "Research and Development of a Hybrid Photo Sensor for a Water Cerenkov Detector," 2004.

[14] T. Abe, *et al.* "Development of Large-Aperture Hybrid Avalanche Photo-Detector," J. Phys. Sco. Jpn. **66**, No. 11, 821 (2011).

[15] H. Nakayama, "Research and Development of a 13-inch Hybrid Avalanche Photo-Detector and its Readout System for a Water Cherenkov Detector," 2006.

[16] H. Nakayama, *et al.*,"Development of a 13-in. Hybrid Avalanche Photo-Detector (HAPD) for a next generation water Cherenkov detector," Nucl. Instrum. Meth. A **567**, 172 (2006).

[17] H. Spieler, "Introduction to Radiation Detectors and Electronics," Lecture Notes - Physics 198, Spring Semester 1998 - UC Berkeley. `http://www-physics.lbl.gov/špieler/physics_198_notes/`.

[18] D. Kollár, "Pulse processing and Analyses," DNP, FMFI UK Bratislava. `http://www.dnp.fmph.uniba.sk/ǩollar/je_w/el3.htm`.